01 Jan 2023

Coaxial Cable Sensing: Review And Perspective

Chen Zhu
Missouri University of Science and Technology, cznwq@mst.edu

Jie Huang
Missouri University of Science and Technology, jieh@mst.edu

Recommended Citation

C. Zhu and J. Huang, "Coaxial Cable Sensing: Review And Perspective," *IEEE Transactions on Microwave Theory and Techniques*, Institute of Electrical and Electronics Engineers, Jan 2023.
The definitive version is available at https://doi.org/10.1109/TMTT.2023.3305049

Coaxial Cable Sensing: Review and Perspective

Chen Zhu, *Member, IEEE*, and Jie Huang, *Senior Member, IEEE*

***Abstract*— The development of sensors has been a hot research topic in both scientific and industrial communities over the past decades. In recent years, a new sensing technology based on coaxial cables has emerged. Inspired by the fiber Bragg grating and motivated by the demand for structural health monitoring, coaxial cable Bragg gratings were first proposed and demonstrated with superior large strain capability (>5%). Mimicking the mature sensing modalities in fiber-optic sensors, coaxial cable sensors are developed to be promising alternatives for fiber-optic sensors in harsh-environment applications involving heavy duty, large strains, high pressures, and high temperatures. Over the past decade, with plenty of efforts being poured into this research direction, a family of coaxial cable sensors with high mechanical robustness, ease of fabrication, high-temperature tolerance, and low system cost have been developed, which has also found wide applications in a diverse array of scenarios, from civil and geological to biochemical engineering. In this article, we provide an overview of reported coaxial cable sensors in the past ten years. Challenges of existing coaxial cable sensing technologies and perspectives on the development of a new generation of ultrasensitive coaxial cable sensors operating at subgigahertz are discussed.**

***Index Terms*— Coaxial cable sensor, coaxial cable, distributed sensing, fiber optic sensor, interferometer, microwave sensor, resonator.**

I. Introduction

OPTICAL fibers and coaxial cables are two types of cylindrical waveguides that have been commonly used for telecommunications. Both optical fibers and coaxial cables can transmit electromagnetic (EM) waves over relatively long distances with acceptable transmission losses, confined by the same EM theory. Yet, the frequencies of the EM waves supported by them are quite different, i.e., optical frequency (e.g., THz) for optical fibers and radio frequency (RF, e.g., GHz) for coaxial cables. Over the past years, optical fibers and coaxial cables have evolved along quite different pathways. Particularly, for example, optical fibers have been extensively exploited for sensing applications in recent years, while coaxial cables are mainly used for RF communications.

Pioneering research has already explored the potential of using coaxial cable devices for sensing applications. Examples include leaky coaxial cables (LCXs), time-domain reflectometry (TDR)-based coaxial cable sensors, and open-ended coaxial probes. An LCX is a type of coaxial cable with periodic slots fabricated on the outer conductor [1]. The propagating EM waves along an LCX radiate outside by these periodic slots, and the radiant electric field can be utilized for radio communication applications in various scenarios, such as underground transportation systems [2], high-speed railways [3], and tunnels [4]. Taking advantage of the radiant electrical field, LCX was used for sensing applications, for example, for target and intrusion detection [5], [6], [7], [8], posture recognition of hospitalized patients [9], and proximity measurement [10]. TDR-based coaxial cable devices were used for measurements of levels and dielectric properties of liquids [11], [12] and distributed crack/strain sensing [13], [14], [15], [16], [17], [18]. Open-ended coaxial probes have been extensively used for the characterization of dielectric properties of various materials at microwave frequencies over the past 40 years [19], [20]. Based on dielectric spectroscopy, a variety of sensing applications of open-ended coaxial probes were demonstrated [21], [22], especially for the dielectric measurement of biological tissues [23]. In this review, these three conventional sensing techniques will not be discussed in detail, while some typical references are provided for the interested reader. Here, we will focus on recently developed coaxial cable sensors over the past ten years that are originally inspired by well-known fiber-optic sensors. Translating the established concepts of fiber-optic sensors and the associated transducer designs into coaxial cables is not only interesting from the perspective of device physics but also attractive because of the potential that the resultant coaxial cable sensors might provide. An overview of the recently developed coaxial cable sensors is given in Fig. 1.

Compared to an optical fiber, a coaxial cable is larger in size dimension and can survive a larger axial strain and shear force. The development of coaxial cable sensors, e.g., the coaxial cable Bragg grating (CCBG) and the coaxial cable Fabry–Perot interferometer (FPI), was inspired by the fiber Bragg grating (FBG) and the fiber-optic FPI, and was motivated by the large strain tolerance of a coaxial cable, which is highly desired in structural health monitoring (SHM) of civil infrastructures [24]. Over the past decade, a variety of coaxial cable sensors have been developed, mimicking their optical counterparts, namely, the fiber-optic sensors, and the application scope of coaxial cable sensors has greatly expanded far beyond SHM. The family of coaxial cable sensors is expected to address the critical issues faced by fiber-optic sensors, such as fragility, the difficulties involved in sensor installation and maintenance, stringent requirements regarding

Manuscript received 30 May 2023; revised 17 July 2023; accepted 29 July 2023. This work was supported by the Research Initiation Project of the Zhejiang Laboratory under Grant 2022ME0PI01. *(Corresponding author: Chen Zhu.)*

Chen Zhu is with the Research Center for Optical Fiber Sensing, Zhejiang Laboratory, Hangzhou 311100, China (e-mail: chenzhu@zhejianglab.com).

Jie Huang is with the Department of Electrical and Computer Engineering, Missouri University of Science and Technology, Rolla, MO 65409 USA.

Color versions of one or more figures in this article are available at https://doi.org/10.1109/TMTT.2023.3305049.

Digital Object Identifier 10.1109/TMTT.2023.3305049

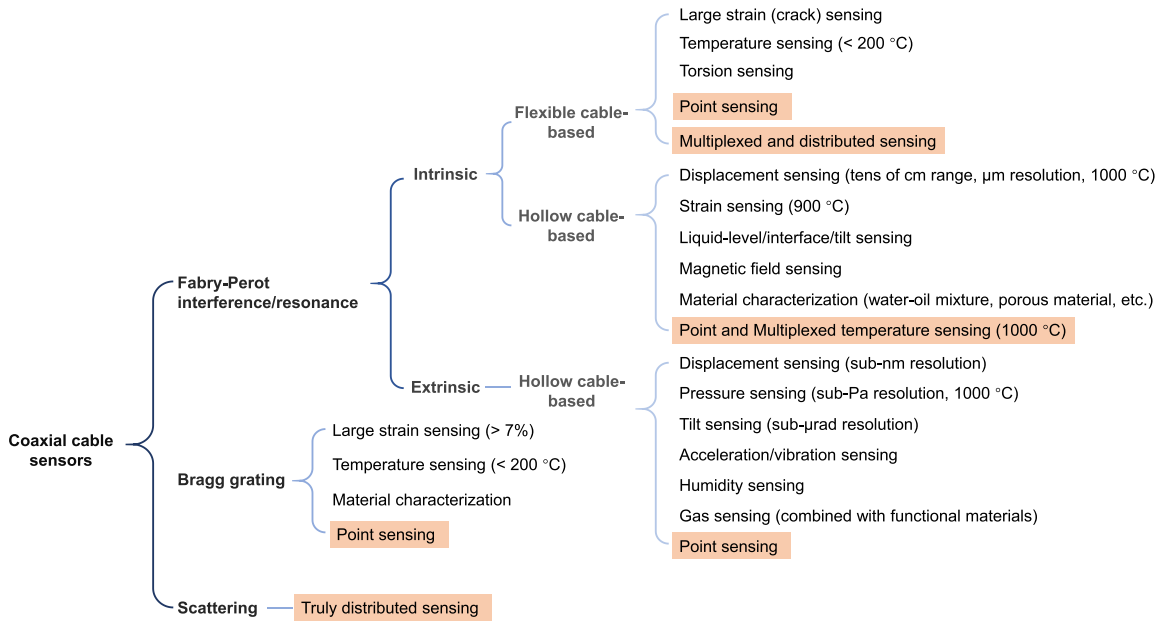

Fig. 1. Overview of the recent development of coaxial cable sensors.

sensor fabrication and alignment, high system cost, and limited applications in high-temperature harsh environments. In this context, the aim of this article is to provide a comprehensive review of the recent progress of coaxial cable sensors.

This article is organized as follows. In Section II, the fundamental physics and applications of the CCBG are reviewed. In Section III, the coaxial cable intrinsic FPIs (CC-IFPIs) are discussed. Section IV reviews the recently developed open-ended coaxial cable resonator-based sensors, i.e., the coaxial cable extrinsic FPIs (EFPIs). In Section V, coaxial cable-based distributed sensing techniques are detailed and followed by a discussion section in Section VI. Section VII concludes this article.

II. Coaxial Cable Bragg Gratings

A. Device Physics

FBGs are one of the most widely used fiber-optic sensors in both scientific and industrial applications [25]. An FBG is fabricated by introducing periodic modulations of the refractive index along the core of an optical fiber. A notch/peak emerges in the transmission/reflection spectrum of an FBG due to the coupling between the forward propagating and the backward propagating core mode. The notch/peak wavelength is the so-called Bragg wavelength, which is uniquely determined by the refractive index of the fiber core and the period of the index modulation. Therefore, strains applied on an FBG can be determined by simply monitoring the shift of its Bragg wavelength, making FBGs an excellent candidate for SHM [26]. The limiting aspect is that FBGs are generally fabricated from silica optical fibers, which are easy to break when it comes to large strains, e.g., >1%, making them unsuitable in extreme scenarios. For example, under extreme loads, such as earthquakes and landslides, the civil infrastructures could experience excessive deformations of up to 10%. Therefore, there is a continuing need for developing new sensor technologies to address the challenges and ensure the safe operation of various infrastructures under extreme conditions. An ideal embeddable strain gauge should have high sensitivity, large dynamic range, excellent reliability, high spatial resolution, and the capability for remote sensing over a long distance and be cost-effective.

Inspired by the FBG and triggered by the demand for large strain measurements in SHM, the CCBG was developed [27], [28]. Fig. 2 presents an overview of the CCBG, including a schematic in Fig. 2(a), a photograph of a drilled open hole in a coaxial cable in Fig. 2(b), and characterization results of the fabricated CCBG using a vector network analyzer (VNA) in Fig. 2(c). As shown in Fig. 2(a), a coaxial cable typically consists of an inner conductor, an outer conductor, and a dielectric layer (e.g., polyethylene). By drilling an open hole into the coaxial cable, an impedance discontinuity was created due to the removal of the local dielectric. By introducing periodic impedance discontinuities along the length of the cable, where each of the discontinuities causes a weak reflection (Γ) of the incident EM wave, a CCBG is formed, similar to an FBG. The constructive accumulation of these weak reflections results in strong reflections at discrete frequencies in the reflection spectrum, corresponding to discrete peaks and notches in the reflection and transmission spectra, respectively, as shown in Fig. 2(c). Interestingly, the resonance frequencies of a CCBG, i.e., the Bragg frequencies, could also be predicted by the phase-matching condition well developed in FBGs [29]

$$f_{\text{res}}^{m} = \frac{mc}{2\Lambda\sqrt{\varepsilon_r}} \tag{1}$$

where m denotes the resonance order; c is the speed of light in vacuum; Λ is the period of the CCBG, namely, the distance between two consecutive holes; and ε_r is the relative permittivity of the dielectric layer. Note that, in addition

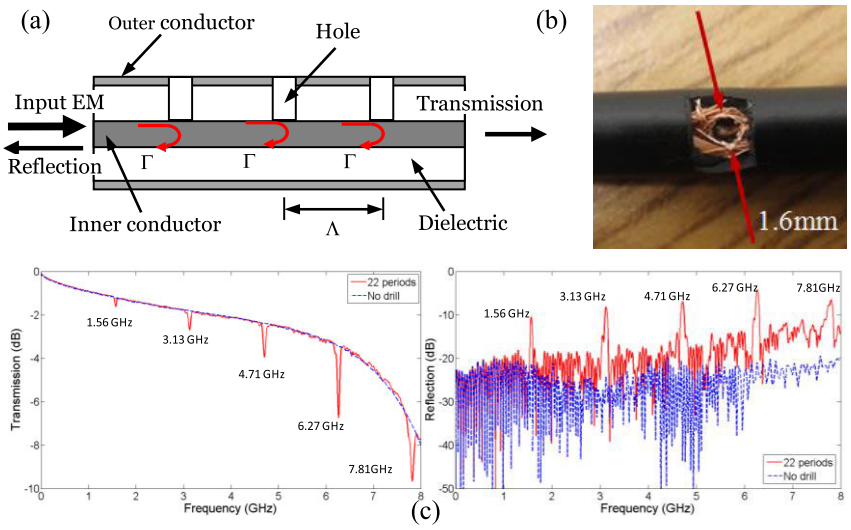

Fig. 2. CCBGs [27]. (a) Schematic. (b) Photograph of the open hole reflector in a coaxial cable. (c) Reflection and transmission spectra of a coaxial cable with and without periodic open holes along the cable.

to the hole-drilling method, ferrule crimping that induces deformations of the coaxial cable is also a common way of creating reflectors along a coaxial cable.

The CCBG is essentially a 1-D photonic crystal structure consisting of periodic impedance discontinuities [30] along the coaxial line. Similar phenomena occur when the microwave signal propagates through these periodic structures to the case where a light signal propagates through an FBG. The forward propagating mode is coupled to the backward propagating mode in the transmission at the discrete Bragg frequencies

$$\beta^{+} - \beta^{-} = \frac{2m\pi}{\Lambda} \tag{2}$$

where β^{+} and β^{-} denote the propagation constants of the forward and backward propagating waves, respectively. Thus, the CCBG also provides a simple method of experimentally investigating EM wave propagation in quasi-periodic and periodic media.

B. Modeling

Complete mathematical models based on transmission line theory, transfer matrix approximation, and coupled-mode theory have been developed to fully understand the CCBG [24], [31], [32]. The transmission line theory-based modeling is easy to understand and is efficient in predicting the resonance frequencies of the device; the transfer matrix method provides a quick path to numerically investigate the reflection and transmission spectra of the device. However, when it comes to more complicated structures, i.e., quasi-periodic and nonuniform structures, these two methods are not applicable. Importantly, the coupled-mode theory-based analysis provides a universal approach to understanding CCBGs with uniform and nonuniform perturbations in the permittivity of the dielectric layer, corresponding to the case where the coupled-mode theory is generalized for studying the transmission and reflection in FBGs. Generally, a coaxial cable is designed for transmitting EM waves in transverse EM (TEM) mode. Therefore, only the coupling between forward and backward TEM waves is considered in the modeling. The coupled wave equation can be expressed as

$$\begin{cases} \dfrac{dA_1}{dz} = -jK\left(A_1 + A_2 e^{j2\beta z}\right) \\ \dfrac{dA_2}{dz} = jK\left(A_1 e^{-j2\beta z} + A_2\right) \end{cases} \tag{3}$$

where A_1 and A_2 are the amplitude of the forward and backward waves; β is the propagation constant of the TEM wave; z is the spatial position along the axial direction of the cable; and K is the coupling coefficient between the forward and backward waves and is given by

$$K = \omega \iint_S dxdy\Delta\varepsilon(x, y, z)|\overline{E(x, y)}|^2 \tag{4}$$

where x and y define the cross section plane of the cable at position z; ω is the angular frequency of the TEM wave; $\Delta\varepsilon(x, y, z)$ is the local change in the permittivity of the cable; and $E(x, y)$ is the modal electric field at the cross section plane. The transfer matrix method based on a finite-difference analysis is employed to solve the coupled wave equation. Assume that the entire coaxial cable with a length of L is segmented into n sections each with a length of Δz, as schematically shown in Fig. 3. The transfer matrix of the EM waves at positions $z(i)$ and $z(i+1)$ is given by

$$\begin{aligned} \begin{bmatrix} A_{1,i+1} \\ A_{2,i+1} \end{bmatrix} &= F_i \begin{bmatrix} A_{1,i} \\ A_{2,i} \end{bmatrix} \\ &= \begin{bmatrix} -jK(i)\Delta z + 1 & -jK(i)e^{2j\beta z(i)}\Delta z \\ jK(i)e^{-2j\beta z(i)}\Delta z & jK(i)\Delta z + 1 \end{bmatrix} \\ &\quad \cdot \begin{bmatrix} A_{1,i} \\ A_{2,i} \end{bmatrix}. \end{aligned} \tag{5}$$

Therefore, the final transfer matrix of an arbitrary grating modified coaxial cable device can be derived as

$$F = F_n \cdot F_{n-1} \cdot \cdots \cdot F_1 = \begin{bmatrix} F_{11} & F_{12} \\ F_{21} & F_{22} \end{bmatrix}. \tag{6}$$

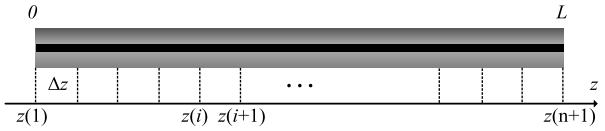

Fig. 3. Schematic of segmentation of a coaxial cable with a length of L along the axial direction, i.e., the z-direction.

Subsequently, the reflection spectrum (S_{11}) of the device, defined as the ratio of the reflected wave to the incident wave at the input port, can be calculated by

$$S_{11} = -\frac{F_{21}}{F_{22}}. \tag{7}$$

The transmission spectrum (S_{21}) can also be calculated by

$$S_{21} = \left(F_{11} - \frac{F_{12} \cdot F_{21}}{F_{22}}\right) e^{-j\beta L}. \tag{8}$$

Note that, here, we only provide a brief review of the coupled-mode theory approach, and a detailed study can be found in [31]. The coupled-mode theory has provided an effective modeling methodology for CCBGs, which can be used to optimize CCBG sensors.

C. Strain Sensing

As the CCBG experiences variations of axial strains, the length of the CCBG and the permittivity of the dielectric layer changes, resulting in shifts of resonance frequencies, according to (1). Specifically, the change in the length (ΔL) and the change in the relative permittivity of the dielectric layer ($\Delta\varepsilon_r^{1/2}$) are given by [33]

$$\begin{cases} \Delta L = L_0 \cdot \varepsilon \\ \Delta\sqrt{\varepsilon_r} = -\dfrac{\varepsilon_r^{3/2}}{2}\left[p_{12} - v(p_{11} + p_{12})\right]\varepsilon = -\sqrt{\varepsilon_r} P_{\text{eff}} \cdot \varepsilon \end{cases} \tag{9}$$

where ε is the strain applied on the CCBG; L_0 is the gauge length of the CCBG; p_{11} and p_{12} are Pockel's coefficients of the dielectric material; v denotes the Poisson ratio of the dielectric material; and P_{eff} is the effective coefficient. Thus, the axial strain-induced shift in the resonance frequency of the CCBG can be expressed as

$$\Delta f = -\left(\frac{\Delta L}{L_0} - \frac{\Delta\sqrt{\varepsilon_r}}{\sqrt{\varepsilon_r}}\right) f_{\text{res}}^m = -(1 - P_{\text{eff}})\varepsilon f_{\text{res}}^m. \tag{10}$$

Thus, increasing tensile strains results in decreases in the resonance frequency. Therefore, the CCBG can be used as a sensor device for strain measurements after proper calibration.

Fig. 4(a)–(c) shows a schematic of the fabrication, a photograph of the strain test setup, and the associated measured responses of a CCBG with a length of 1 m and a grating period of 25 mm to variations of applied axial tensile strains, respectively. A VNA is connected to the CCBG so that the fabrication process can be monitored in real time. In the strain test, the CCBG was mounted on a heavy-duty material tester, and the S_{11} parameter on the VNA was recorded for each applied strain. The corresponding resonance frequency was then extracted from the magnitude coefficient of the measured

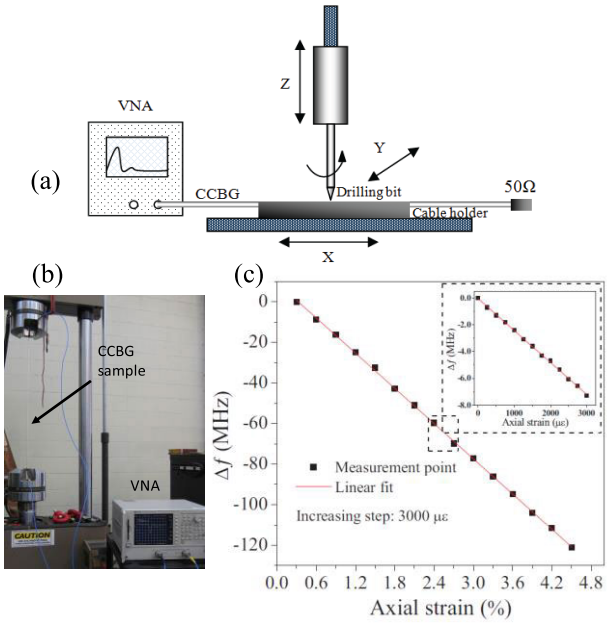

Fig. 4. CCBG strain sensor [24]. (a) Schematic of the CCBG fabrication. (b) Photograph of the strain test setup. (c) Large-strain responses of a prototype CCBG. The inset shows an enlarged view of the selected section where the strain was increased with a step size of 300 $\mu\varepsilon$.

S_{11} (i.e., reflection spectrum). The CCBG was demonstrated to survive up to 5% with a sensitivity of -2.1 kHz/$\mu\varepsilon$ [24]. Advanced signal processing techniques, such as cross correlation, were used to analyze the measured reflection spectra of the CCBG, and an improved resolution of 100 $\mu\varepsilon$ was verified [34]. The large dynamic range and linear response of the CCBG provide a viable solution to SHM where measurements of extremely large strains are needed.

Additional efforts have been made in the development of cost-effective interrogation units for the CCBG sensor to replace the benchtop VNA. Inspired by the FBG-based fiber ring laser sensor [35], an RF positive feedback system was proposed to enhance the quality-factor (Q-factor) of the CCBG signal and ultimately improve the limit of detection of the CCBG sensor [36]. Fig. 5(a) gives a schematic of the interrogation system. By carefully tuning the passband of the filter and the gain coefficient of the amplifier, the signal at the resonance frequency of the CCBG can oscillate, while the signals at other frequencies are suppressed because the Barkhausen conditions are not satisfied. Fig. 5(b) shows a measured output spectrum of the system, where a remarkably enhanced Q-factor of 17 729 (3500 times larger than that of the CCBG itself) is revealed. Fig. 5(c) shows the measured responses of the system when axial strains in steps of 20 $\mu\varepsilon$ were applied. The limit of detection of the positive feedback system-interrogated system was also improved by a factor of 5 compared to the conventional VNA-interrogated CCBG. By employing another CCBG as the reference, a low-cost two CCBG-sensor system with a portable spectrum analyzer was demonstrated [37], paving the way to future large-scale field deployment of CCBG sensors.

Note that the CCBG is also sensitive to temperature variations due to the effect that the relative permittivity of the

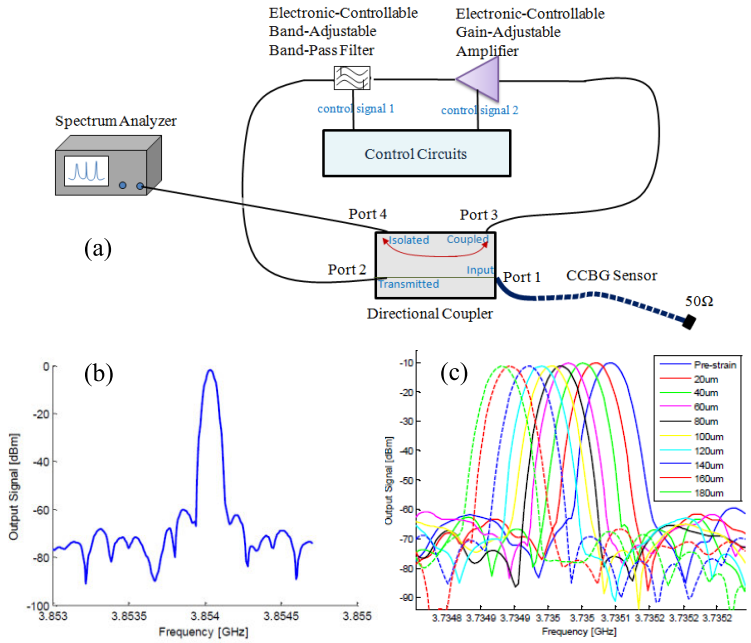

Fig. 5. Positive feedback system interrogated CCBG strain sensor [38]. (a) Schematic of the system. (b) Output signal with an enhanced Q-factor of 17 729. (c) Measured responses for different settings of axial strains in steps of 20 $\mu\varepsilon$.

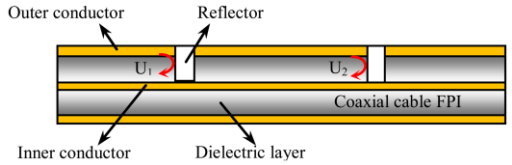

Fig. 6. Schematic of a CC-IFPI [42].

dielectric layer varies at different temperatures. It is shown that a semirigid CCBG is less sensitive to temperature than a flexible CCBG (e.g., made of RG-58), making it a promising candidate for temperature-insensitive strain measurements in SHM [38]. By implementing the Bragg structure in air-filled coaxial waveguides, the resultant devices were used for material characterization [39], [40], [41].

III. Coaxial Cable Intrinsic Fabry–Perot Interferometers

A. Flexible Cable-Based

1) Low-Finesse Fabry–Perot Cavity: Although the CCBG showed great potential for large strain sensing, the spatial resolution of a CCBG sensor is limited due to its long gauge length (on the order of several tens of cm). To address this issue, the CC-IFPI was developed [42]. The idea of the CC-IFPI came from the fiber-optic IFPI, where only two fiber-line reflectors with a distance of sub-mm are required to form a micro Fabry–Perot cavity that can be used for sensing applications, e.g., measurements of temperature and strain [43]. A schematic of the CC-IFPI is shown in Fig. 6. Two open hole-based reflectors are fabricated along a coaxial cable, and a microwave Fabry–Perot cavity interferometer is formed between the two reflectors. The interference signal of the CC-IFPI is the summation of the two reflected waves at the two reflectors, namely, U_1 and U_2, as indicated in Fig. 6, assuming that the reflectivity of the two reflectors is low. The magnitude of the interference signal is given by [42]

$$U = 2 \cdot \Gamma(f) e^{-\alpha z} \cos\left(\frac{4\pi f L\sqrt{\varepsilon_r}}{c}\right) \tag{11}$$

where $\Gamma(f)$ represents the reflection coefficient magnitude of the hole reflector, which is frequency-dependent; f is the probing microwave frequency; L is the distance between the two reflectors, i.e., the cavity length of the Fabry–Perot cavity; and c is the speed of light in vacuum. Equation (11) essentially describes a sinusoidal waveform that is known as an interferogram in fiber-optic IFPI sensors.

2) Strain and Temperature Sensing: Fig. 7 shows the numerical and experimental characterization results of a prototype CC-IFPI with a gauge length of 7 cm fabricated from a flexible RG-58U cable. The reflection coefficient magnitude of the hole reflector was first obtained via full-wave simulation, as given in Fig. 7(a). The reflection spectrum of the CC-IFPI was then calculated based on (11) and is shown in Fig. 7(b), where the measured spectrum is also plotted for comparison. Discrete resonance frequencies could be observed, similar to those of fiber-optic IFPIs, which can be expressed as (neglecting the phase variations at the hole reflectors)

$$f_m = \frac{mc}{2d\sqrt{\varepsilon_r}} \tag{12}$$

where m is an integer denoting the resonance order; d is the distance between the two reflectors (i.e., the cavity length); and ε_r is the relative permittivity of the dielectric layer of the coaxial cable. The measured and calculated reflection spectra match well, validating the proposed model shown in (11). The discrete resonance frequencies can be tracked for sensing applications. Specifically, an applied tensile strain results in a

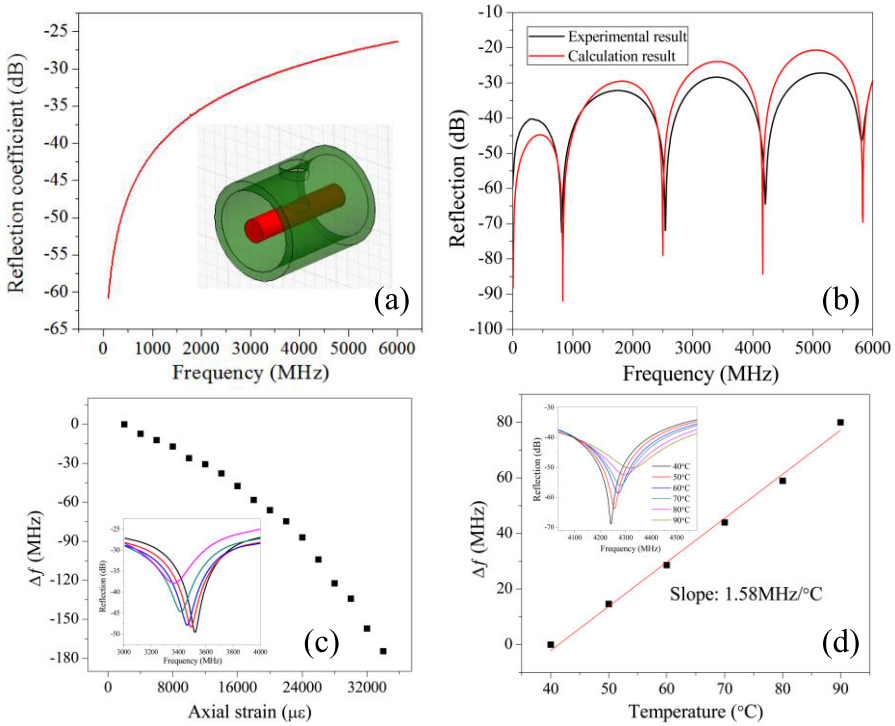

Fig. 7. Characterization of a CC-IFPI based on a flexible cable [42]. (a) Reflection coefficient magnitude of the hole reflector. (b) Calculated and measured interferograms of a 7-cm CC-IFPI. (c) Strain responses. The inset shows the evolution of the reflection spectra as applied axial strain increased. (d) Temperature responses. The inset shows the evolution of the reflection spectra as temperature increased from 40 °C to 90 °C.

change in the relative permittivity of the dielectric layer and a change in the cavity length, therefore leading to a change in the resonance frequency according to

$$\Delta f_m = \frac{\partial f_m}{\partial d}\Delta d + \frac{\partial f_m}{\partial \varepsilon_r}\Delta \varepsilon_r. \tag{13}$$

Thus, the applied strain (ε) can be inferred from the measured change in the resonance frequency

$$\varepsilon = \frac{2\Delta f_m}{f_m(P_{\text{eff}} - 2)} \tag{14}$$

where P_{eff} denotes the effective Pockels coefficient of the dielectric material. According to (14), a higher resonance frequency will lead to a larger measurement sensitivity. In a proof of concept, strain sensing was demonstrated by tracking the shifts of the resonance frequency at ~4 GHz, as shown in Fig. 7(c). The resonance frequency shifted to the low-frequency regime with increasing strains due to the elongation of the cavity length, which matches well with the response of the CCBG shown in Fig. 4. The temperature crosstalk was also investigated, as given in Fig. 7(d), which was mainly attributed to the dependence of the permittivity of the dielectric layer of the cable on temperature. Compared to the CCBG, the CC-IFPI is featured in its smaller gauge length. The low reflectivity of the CC-IFPI also provides small insertion losses. Therefore, a series of such CC-IFPIs can be cascaded for spatially distributed sensing, taking advantage of the phase measurement capability at microwave frequencies, as discussed in Section V.

B. Hollow Cable-Based

1) Hollow Coaxial Cable Design: The CC-IFPI and CCBG sensors fabricated from commercial flexible coaxial cables were demonstrated for measurements of large strains, providing a complement to fiber-optic sensors in SHM. Another limiting aspect of fiber-optic sensors is their high-temperature applications due to the intrinsic material property of silica fibers. Although sapphire fibers have been developed for high-temperature applications, the sensing performances of sapphire fiber sensors are not yet on par with silica fiber sensors due to the highly multimodal nature and high cost of sapphire fibers [44], [45]. Thus, the development of a novel sensing platform suitable for ultrahigh-temperature environments (e.g., >1000 °C) is highly desired to meet the demands in various applications, such as aerospace and energy industries.

The temperature tolerance of the developed CC-IFPI and CCBG sensors is compromised due to the material limitation attributed to the dielectric layer, for example, polyethylene, which typically operates below 200 °C. Therefore, Trontz et al. [46] reported a custom metal-ceramic coaxial cable (MCCC) as the platform to improve the temperature performance of coaxial cable sensors. The conductors of the MCCC were fabricated using stainless steel, and alumina was used as the dielectric material. Microwave IFPIs were fabricated from the custom coaxial cable by introducing two air-gap reflectors along the coaxial line. The resultant MCCC-IFPIs were demonstrated for temperature measurements in the range of 200 °C–500 °C. The long-term stability and responses of the MCCC-IFPIs at temperatures above 500 °C were not investigated. However, the fabrication of the MCCC-IFPIs required

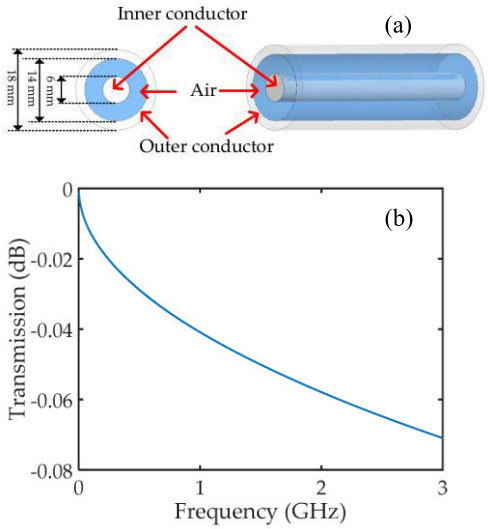

Fig. 8. HCC [47]. (a) Schematics of the designed prototype HCC. (b) Full-wave simulated transmission loss of an 11.8-cm-long HCC with respect to frequency.

multiple assembly processes and involved multiple different materials, which might detrimentally affect the mechanical and thermal stability of the sensor devices. Nevertheless, the demonstration of the MCCC-IFPIs opened new avenues for developing high-temperature coaxial cable sensors that could be used as an alternative to fiber-optic sensors for applications in high-temperature harsh environments.

Later, a simple hollow coaxial cable (HCC), as a new high-temperature sensing platform, was proposed and demonstrated [47]. The idea of the HCC is to remove the conventional dielectric material and use the sandwiched air in-between the inner and outer conductors as the insulation layer. Meanwhile, stainless steel is used to fabricate the conductors to ensure their robustness. Schematics of a prototype HCC are given in Fig. 8(a). The dimensional sizes of the HCC are carefully designed to ensure that the characteristic impedance of the HCC is 50 Ω, matching widely used commercial cables so that sensing signal transmission would be easy. Fig. 8(b) shows the full-wave simulated transmission loss of an 11.8-cm-long HCC, showing an acceptable low loss coefficient.

2) Fabry–Perot Resonator: It is worth noting that the reflection along the coaxial cable length (caused by imperfect cable manufacturing) might degrade the signal-to-noise ratio (SNR) of the reflection spectrum of a CC-IFPI due to the weak reflectivity of the pair reflectors in the CC-IFPI design. Therefore, to ensure a high SNR, additional signal processing, including the Fourier transforms and filtering, must be performed to obtain a clean interferogram from a CC-IFPI that facilitates high-performance sensing [42]. Note that the spectra shown in Fig. 7(b) were postprocessed. On the other hand, the low reflectivity of the pair reflectors also results in a low Q-factor of a CC-IFPI, which detrimentally affects the measurement resolution of the sensor device. Therefore, it is straightforward to increase the reflectivity of the pair reflectors in a CC-IFPI to address these two issues. According to transmission line theory, there are many ways to create a reflector with high reflectivity in a coaxial cable [48]. Ahmed et al. [49] reported a high Q-factor coaxial cable Fabry–Perot resonator (CC-FPR) for sensing applications. A pair of high-reflectivity reflectors was created by first drilling two open holes along a commercial flexible coaxial cable and then filling the open holes with copper powder. The resultant resonating structure between the two reflectors significantly increased the Q-factor by ten times, and concomitantly, a relative resolution of 4×10^{-6} was demonstrated. Meanwhile, the reflection spectrum of the CC-FPR could be directly measured for sensing applications without any additional signal processing that is encountered by the CC-IFPIs.

With the implementation of the resonating structure on an HCC, a new sensing configuration, the HCC Fabry–Perot resonator (HCC-FPR), was demonstrated recently [50]. A schematic representation of the HCC-FPR is shown in Fig. 9(a). Compared to the MCCC-IFPI, the all-metal and assembly-free structure design of the HCC-FPR provides enhanced thermal and mechanical robustness. The fabrication of the HCC-FPR only involves standard metal welding and cutting procedures, which are cost-effective. The first reflector of the HCC-FPR is a metal post that is welded within the HCC at the RF input end, shorting the inner and outer conductors. The short circuit results in a rise to the storage of magnetic field energy near the post, causing a high reflection of the incident EM waves and, thus, serving as a high-reflectivity reflector. From the point of view of an equivalent circuit, the metal post can be considered as a shunt inductor and a series shunt resistor. The reflection coefficient of the metal post in a small frequency range (e.g., <3 GHz) can then be expressed as [51]

$$\begin{cases} r_1 = \Gamma_1 e^{j\phi_1} = \dfrac{R + j\omega L - Z_0}{R + j\omega L + Z_0} \\ \phi_1 = \pi - \tan^{-1}\dfrac{\omega L}{Z_0 - R} - \tan^{-1}\dfrac{\omega L}{Z_0 + R} \end{cases} \tag{15}$$

where Γ_1 and ϕ_1 denote the reflection coefficient magnitude and phase, respectively; R and L are the resistance and inductance of the metal post in the equivalent circuit model; ω is the angular frequency of the signal; and Z_0 is the characteristic impedance of the HCC. An additional capacitor component needs to be taken into account for high-frequency signals. The second reflector is a circular metal sheet that also shorts the inner and outer conductors. The same model shown in (15) applies to the reflection coefficient of the metal sheet (i.e., r_2, Γ_2, and ϕ_2). Fig. 9(b) and (c) shows the full-wave simulated reflection coefficient magnitude of the first and second reflectors, respectively. Both reflectors show high reflectivity to the EM waves due to the short circuit, and the reflectivity decreases as the frequency increases.

From the perspective of multiple reflections of a microwave signal in the cavity, the reflection coefficient of the HCC-FPR is given by [51]

$$\begin{aligned} r &= \frac{r_1^* - r_2 e^{-\alpha 2d - j\delta}}{1 - r_1 r_2 e^{-\alpha 2d - j\delta}} \\ &= \frac{\Gamma_1 e^{-j\phi_1} - \Gamma_2 e^{j\phi_2} e^{-\alpha 2d - j\delta}}{1 - \Gamma_1 e^{-j\phi_1} \Gamma_2 e^{j\phi_2} e^{-\alpha 2d - j\delta}} \end{aligned} \tag{16}$$

where α is the transmission loss coefficient of the HCC; d is the cavity length of the resonator, i.e., the distance between

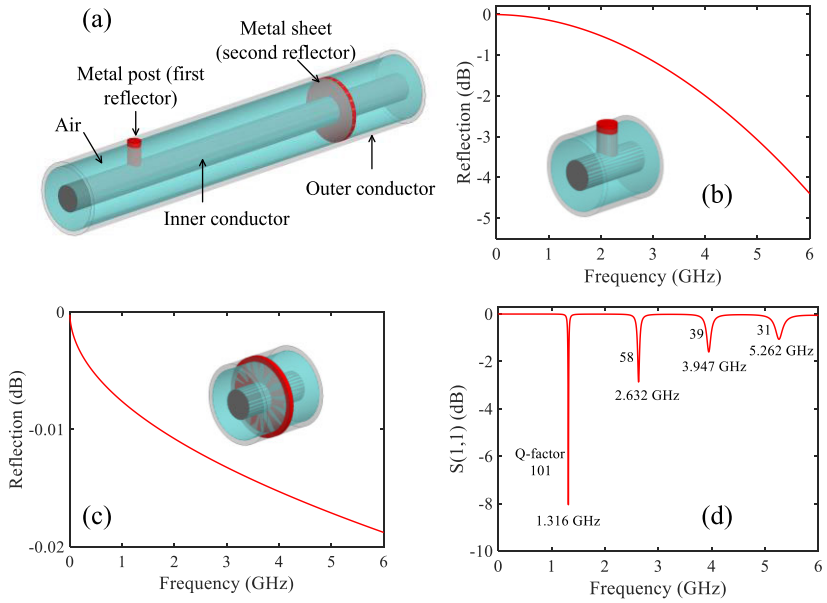

Fig. 9. HCC-FPR [50]. (a) Schematic of the HCC-FPR. (b) Reflection coefficient magnitude of the metal post reflector. (c) Reflection coefficient magnitude of the metal sheet reflector. (d) Reflection coefficient magnitude of the HCC-FPR with a cavity length of 11.4 cm.

the two reflectors; c is the speed of light in vacuum; and $\delta = \frac{4\pi\sqrt{\varepsilon_0}df}{c}$ denotes the round-trip phase delay of the cavity. The superscript asterisk "$*$" denotes the complex conjugate. The reflection coefficient magnitude (i.e., the resonance reflection spectrum) of the HCC-FPR can be expressed as

$$M = \sqrt{\frac{\Gamma_1^2 - 2\Gamma_1\Gamma_2 e^{-\alpha 2d}\cos(\delta - \phi_1 - \phi_2) + \Gamma_2^2 e^{-\alpha 4d}}{1 - 2\Gamma_1\Gamma_2 e^{-\alpha 2d}\cos(\delta - \phi_1 - \phi_2) + \Gamma_1^2\Gamma_2^2 e^{-\alpha 4d}}}. \tag{17}$$

The resonance frequencies of the HCC-FPR can be calculated by equating the phase-matching condition

$$f_m = \frac{c(2m\pi + \phi_1 + \phi_2)}{4\pi\sqrt{\varepsilon_0}d} \tag{18}$$

and the resonance wavelength can be expressed as

$$\lambda_m = \frac{4\pi\sqrt{\varepsilon_0}d}{2m\pi + \phi_1 + \phi_2} \tag{19}$$

where m is a nonnegative integer denoting the resonance order. As can be seen from (19), the resonance wavelength is linearly proportional to the cavity length, given that ϕ_1 and ϕ_2 can be considered constant in a small frequency range. Substituting the full-wave simulated reflection coefficients of the two reflectors into (17), the reflection spectrum of the HCC-FPR can be calculated, as shown in Fig. 9(d). Four resonance dips, including the fundamental resonance and three high-order harmonics, can be observed with significantly enhanced Q-factors compared to the CC-IFPI with a typical Q-factor of 5. It is also interesting to see that the resonance depth of the four dips decreases with increasing frequencies. This is because the reflectivity of the two reflectors becomes more unbalanced in the high-frequency region.

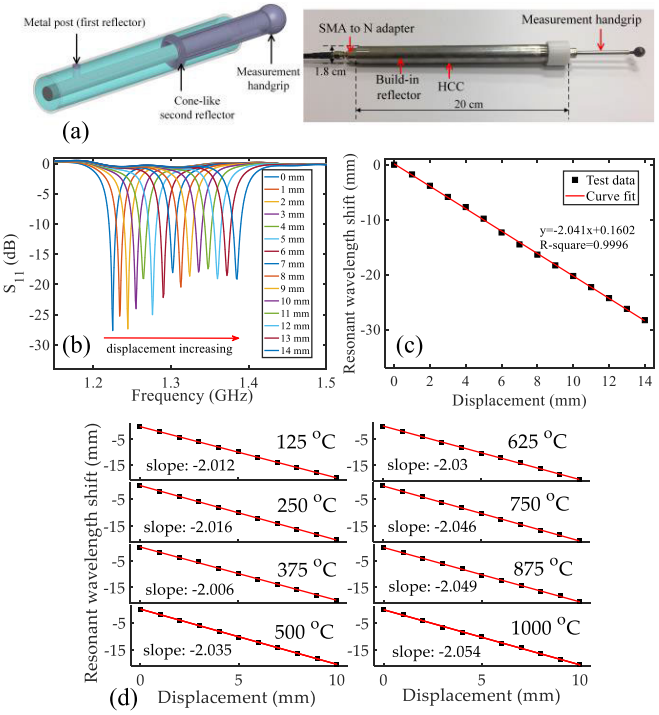

Fig. 10. HCC-FPR large-range, high-linearity, and high-temperature displacement sensors. (a) Schematic and photograph of a displacement sensor [50]. (b) Evolution of the reflection spectra of the sensor for different settings of displacement. (c) Change in the fundamental resonant wavelength of the sensor as a function of displacement. (d) Shift in the resonant wavelength as a function of displacement over a displacement range of 10 mm at eight different temperature settings (125 °C–1000 °C with a step of 125 °C). Linear curve fitting was applied to the test data, and the slopes are indicated in the figure.

3) HCC-FPR Sensing Applications: Based on the HCC-FPR approach, we recently reported a series of robust and low-cost coaxial cable sensors that can be potentially used

in high-temperature harsh environments for the measurements of displacement, strain, liquid level, and so on. According to (18) and (19), the resonance frequencies (wavelengths) of an HCC-FPR are directly dependent on the cavity length of the Fabry–Perot cavity. Therefore, any physical quantities that can be correlated with the cavity length can be measured using the HCC-FPR platform. For example, we demonstrated a wide-range displacement sensor based on an HCC-FPR [50], [52]. Fig. 10(a) shows a schematic and a photograph of the prototype sensor made of stainless steel. The second reflector of the HCC-FPR displacement sensor is made movable and is connected to a measurement handgrip. The movements of the handgrip directly change the cavity length of the Fabry–Perot cavity and, thereby, can be monitored by tracking the resonance wavelength/frequency of the HCC-FPR. The linear dependence of the resonance wavelength of the prototype sensor on variations of displacements over a range of 0–14 mm was demonstrated, as shown in Fig. 10(b) and (c). It was observed that the resonance depth generally decreased with increasing resonance frequencies as expected because the reflectivities of the two reflectors of the resonator become more unbalanced at higher frequencies [see Fig. 9(b) and (c)]. Slightly inconsistent variations of the resonance depth were also shown, which are due to the fact that, during the displacement experiment, the physical contact between the cone-like second reflector and inner/outer conductors gently varies as it is pushed inward. The slight changes in the physical contact vary the effective reflectivity of the second reflector, resulting in inconsistent variations in the resonance depth. The resolution was also investigated and demonstrated to be approximately 1 μm. More importantly, measurements of displacements using the HCC-FPR sensor at elevated temperatures up to 1000 °C were conducted, showing consistent responses at various temperature settings, as shown in Fig. 10(d) [53]. As an application demonstration, the high-temperature HCC-FPR displacement sensor was also employed to measure the thermal strains of a steel plate during the heating process up to 900 °C.

An HCC-FPR-based wide-range and high-resolution liquid-level sensor was also reported [54]. Fig. 11(a) presents a schematic and a photograph of the liquid-level sensor. In the design of the liquid-level sensor, the air–liquid interface is employed as the second reflector, and thereby, variations of the liquid levels are directly encoded into the changes in the Fabry–Perot cavity, similar to the displacement sensor shown above. The measured reflection spectra of the sensor for different settings of liquid levels are given in Fig. 11(b). The sensor showed a linear response over a dynamic range of 200 mm in terms of resonant wavelength, as shown in Fig. 11(c). From the stair-step characterization shown in Fig. 11(d), a maximum deviation in the resonant wavelength is determined to be 2.4 μm (unit: wavelength), corresponding to a measurement uncertainty of 5.0 μm (unit: liquid level). The temperature insensitivity of the prototype sensor device was also experimentally verified. Due to its all-metal structure (i.e., high-temperature stability), it could be used for high-temperature applications, for example, in situ monitoring the levels of molten metal in the steelmaking industry. Inspired

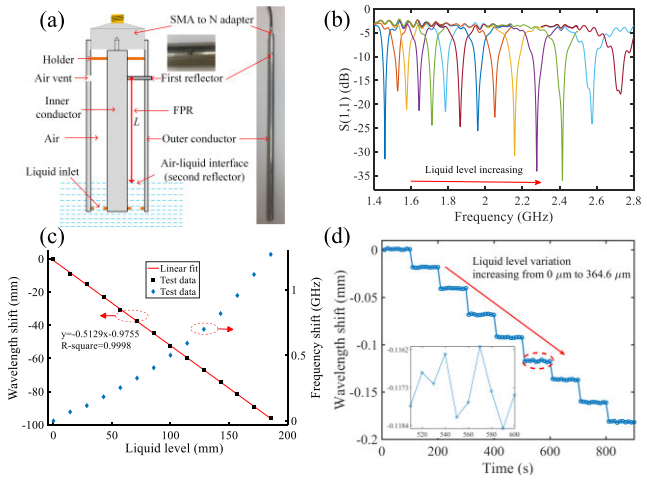

Fig. 11. HCC-FPR liquid level sensor [54]. (a) Schematic and photograph of the liquid-level sensor. (b) Measured spectral responses with increasing liquid levels. (c) Resonant wavelength shift and frequency shift as a function of liquid level. (d) Shift in the resonance wavelength of the liquid-level sensor with respect to small variations of the liquid level. The inset plots the wavelength shift deviation in the time period of 500–600 s, showing a maximum deviation of 2.4 μm.

by the liquid-level sensor design, an HCC-FPR pair-based temperature-insensitive inclinometer was recently reported [55]. The tilt angle is correlated with the liquid level in the HCC-FPR and, therefore, can be measured by quantifying shifts in the resonance wavelength. Importantly, in the sensor design, two HCC-FPRs are used to eliminate crosstalk induced by temperature variations.

The hollow cavity of the HCC-FPR gives us the opportunity to characterize the dielectric properties of the material filled in the cavity. Thus, in addition to measurements of cavity length-related physical parameters, the HCC-FPR was also developed for measurements of dielectric properties of materials at microwave frequencies [56], [57], [58]. By directly filling the liquid analyte in the hollow cavity, a high-sensitivity liquid dielectric constant sensor was demonstrated [56]. Fig. 12(a) gives a schematic and a photograph of the prototype sensor. Similar to the liquid-level sensor design, the air–liquid interface serves as the first reflector, together with the metal disk reflector, forming a resonator, whose resonance is dependent on the dielectric constant of the liquid filled in the cavity. By correlating the position of the liquid interface in a multilayer liquid system to the effective dielectric constant of an HCC-FPR, a contactless liquid interface sensor was reported, as shown in Fig. 12(b) [59]. The noncontact working fashion of the HCC-FPR sensor might make it attractive when dealing with conductive, corrosive, or chemically active liquids. In addition to the HCC-FPR, the hollow cavity-based MCCC-IFPI was also explored for the characterization of the relative permittivity of different solid and liquid materials [60]. By engineering an inlet and an outlet port on an MCCC-IFPI, continuously monitoring dielectric constants of pure and mixed liquids was achieved, as shown in Fig. 12(c) [57]. Compared to the HCC-FPR configuration, additional signal processing is required to extract the reflection spectrum of the FPI for analysis. Zeng et al. [61] also employed an MCCC-IFPI

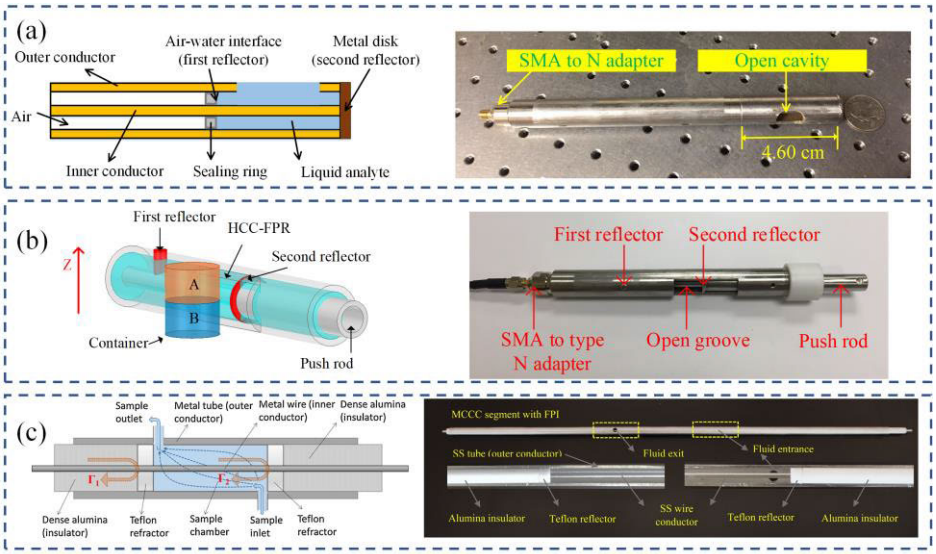

Fig. 12. HCC-FPR- and MCCC-IFPI-based sensors. (a) HCC-FPR liquid dielectric constant sensor [56]. (b) HCC-FPR liquid interface sensor [59]. (c) MCCC-IFPI liquid dielectric constant sensor [58].

platform to characterize the molecular adsorption-dependent dielectric properties of zeolite, demonstrating a convenient and reliable means for chemical applications. By filling the hollow cavity of an MCCC-IFPI with a magnetic fluid whose dielectric constant varies with the strengths of the magnetic field, a linear-response magnetic fluid sensor was reported [58]. Indeed, the preliminary investigations indicate that it would be promising to develop robust, portable, and low-cost HCC-FPR-based chemical gas sensors by filling the hollow Fabry–Perot cavity with functional materials, e.g., zeolite and metal-organic framework (MOF) [62].

IV. Coaxial Cable Extrinsic Fabry–Perot Interferometers

Despite great efforts that have been put into the development of coaxial cable devices, the sensors mentioned above (IFPI-based) all suffer from low measurement resolution compared to their fiber-optic counterparts (i.e., fiber-optic IFPI). In addition, the structural design flexibility of the MCCC-IFPI and HCC-FPR is still limited due to the inherently intrinsic configuration, hindering the expansion of the application scope of coaxial cable sensors. Very recently, we reported a novel and ultrasensitive microwave sensing platform, named the open-ended HCC resonator (OE-HCCR), which successfully overcomes the issues faced by previously existing coaxial cable sensors, i.e., low measurement resolution and low degree of freedom in sensor design. The OE-HCCR is reviewed in detail in this section.

A. Principle

Open-ended coaxial probes have evolved to the status of a "go-to" tool for the determination of EM properties of the material under test (MUT) at microwave frequencies [23]. The fringing electric field of the open-ended coaxial cable penetrates the MUT (dielectric material) in front of the end facet of the probe and interacts with the MUT, and thereby, the complex permittivity of the MUT is correlated with the reflection coefficient in both magnitude and phase of the coaxial probe. It was reported that the response of an open-ended probe varies when the MUT is backed by air or a conducting plate [63], [64]. From the point of view of an equivalent circuit, a simple explanation for the different responses is that the fringing capacitance of the probe varies in two different circumstances. Interestingly, the fringing capacitance increases exponentially as the conducting plate approaches the probe tip [64], and the exponential dependence essentially provides a scheme to obtain an ultrahigh measurement sensitivity using an open-ended coaxial line. So far, most of the open-ended coaxial probes are used for dielectric spectroscopy. However, from another perspective, we have noted that the open-ended coaxial probe is inherently an analogy of a fiber-optic EFPI. Therefore, motivated by the fiber-optic EFPI, a new microwave device, named the OE-HCCR (i.e., the coaxial cable EFPI), was developed [65]. A schematic illustration of the OE-HCCR is shown in Fig. 13. The OE-HCCR integrates the strength from both the open-ended coaxial probe and interferometry. The Fabry–Perot cavity of the OE-HCCR is formed between the metal post and the open-end reflector. The fundamental basis of the OE-HCCR for sensing applications relies on the dependence of the capacitance over its open-end aperture on the *pseudo* cavity length, defined as the gap distance between the open end and the metal plate [51]. Specifically, the fringing electric field excited static capacitance over the aperture can be expressed as [64]

$$C = C_1 + C_2 \tag{20}$$

where

$$C_1 = \frac{2\varepsilon_0}{\left[\ln(b/a)\right]^2} \int_a^b \int_a^b \int_0^\pi \frac{\cos\phi' d\rho d\rho' d\phi'}{\sqrt{\left[\rho^2 + \rho'^2 - 2\rho\rho'\cos\phi'\right]}} \tag{21}$$

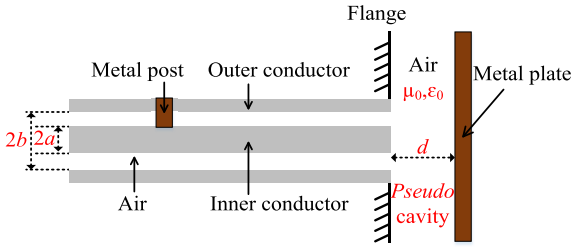

Fig. 13. Schematic of the OE-HCCR [51].

and

$$C_2 = \frac{4\varepsilon_0}{\left[\ln(b/a)\right]^2}\sum_{n=1}^{\infty}\int_a^b\int_a^b\int_0^{\pi} \times \frac{\cos\phi' d\rho d\rho' d\phi'}{\sqrt{\left[\rho^2+\rho'^2+4n^2d^2-2\rho\rho'\cos\phi'\right]}} \quad (22)$$

where ρ and ρ' denote the radial direction and ϕ' denotes the azimuthal direction. The capacitance at the open end of the OE-HCCR exhibits an exponential dependence on the *pseudo* cavity length of the OE-HCCR [51]. The changes in the *pseudo* cavity length results in changes in the reflection coefficient phase of the open-end reflector (ϕ_2) based on [51]

$$\begin{cases} r_2 = \Gamma_2 e^{j\phi_2} = \dfrac{1-j\omega Z_0 C}{1+j\omega Z_0 C} \\ \phi_2 = -2\tan^{-1}(\omega Z_0 C) \end{cases}. \quad (23)$$

Subsequently, the variations of ϕ_2 lead to shifts in the resonance frequency of the OE-HCCR according to (18). Thus, changes in the *pseudo* cavity length of the OE-HCCR are encoded in the changes in its resonance frequency. Therefore, by monitoring the resonance frequency, an OE-HCCR can be employed as a sensor device (e.g., displacement sensor) after proper calibration.

B. Concept Validation

Characterizations of a prototype OE-HCCR are presented in Fig. 14. The size dimensions of the prototype OE-HCCR [as shown in the inset of Fig. 14(a)] are smaller than the HCC-FPR as reviewed above. The characteristic impedance is also designed to be 50 Ω to match that of commercial flexible coaxial cables. Fig. 14(a) gives the measured reflection spectrum of the OE-HCCR showing the fundamental resonance dip. The setup employed to investigate the response of the OE-HCCR to changes in its *pseudo* cavity length is given in Fig. 14(b). As can be seen in Fig. 14(c), the reflection spectrum shifted to the high-frequency region as the *pseudo* cavity length increases, and the determined resonance frequency as a function of the *pseudo* cavity length is shown in Fig. 14(d). The resonance frequency decreases exponentially as the *pseudo* cavity length decreases, and the sensitivity increases exponentially as the *pseudo* cavity length decreases. The sensitivity reaches 7 GHz/mm as the *pseudo* cavity length was set to 0.1 mm, an unprecedented sensitivity among coaxial cable sensors. The exponential dependence of the OE-HCCR on the *pseudo* cavity length provides a new scheme that could be used for ultrasensitive sensing applications.

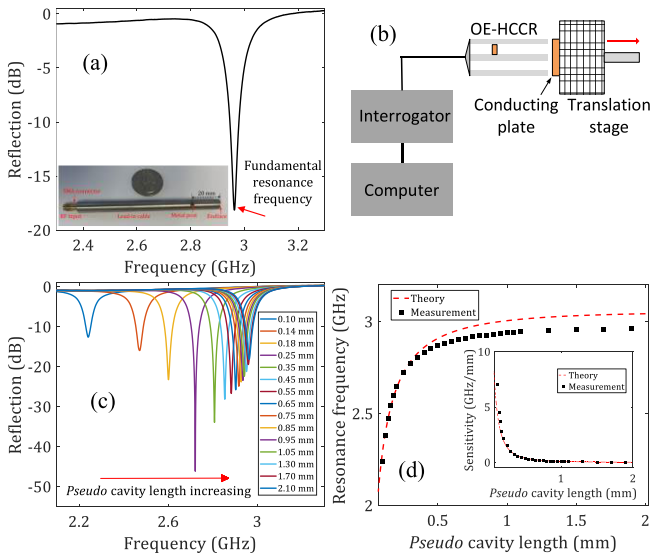

Fig. 14. Characterizations of a prototype OE-HCCR [65]. The diameters of the inner conductor and outer conductor of the HCC are 2.2 and 5.0 mm, respectively. The distance between the metal post and the open end of the coaxial line is 20.0 mm. (a) Measured reflection spectrum. The inset shows a photograph of a prototype. (b) Experimental setup. (c) Evolution of the reflection spectra for different settings of the *pseudo* cavity length. (d) Resonance frequency as a function of the *pseudo* cavity length. The plot of the sensitivity with respect to *pseudo* cavity length is shown as an inset. Both measured results and theoretically calculated results are included for comparison.

C. Sensing Applications

The extrinsic configuration of the OE-HCCR greatly facilitates the development of OE-HCCR-based sensor devices and gives us the opportunity to develop a series of new ultrasensitive microwave sensor devices, mimicking the well-established concepts and sensor designs in fiber-optic EFPI sensors. A detailed comparison between the OE-HCCR technique and fiber-optic EFPI can be found in [51]. The section reviews the recently reported sensors developed based on the OE-HCCR principle.

An OE-HCCR-based accelerometer (a vibration sensor) was developed with the assistance of an inertial mass block mounted at the open end of the OE-HCCR via a thin metal beam, as shown in Fig. 15(a) [66]. Inertial movements of the mass block due to accelerations result in changes in the deformation of the thin beam, leading to variations of the effective gap distance between the mass block and the open end of the coaxial cable, which can be accurately captured by the OE-HCCR with high sensitivity [66]. Meanwhile, a new signal demodulation approach was proposed, where the interrogation frequency is determined from the quasi-linear point from the reflection spectrum (in dB) of the sensor device, as indicated in Fig. 15(b). By monitoring changes in the magnitude of the signal at the operating frequency, instantaneous vibrations of the mass block can be tracked, as shown in Fig. 15(c). The single-frequency approach provides a much faster update rate compared with the full-spectrum measurement. However, the nonlinear response limits the dynamic range of the sensor. In addition, thanks to the high sensitivity of the OE-HCCR sensor, an interesting application of the prototype device for

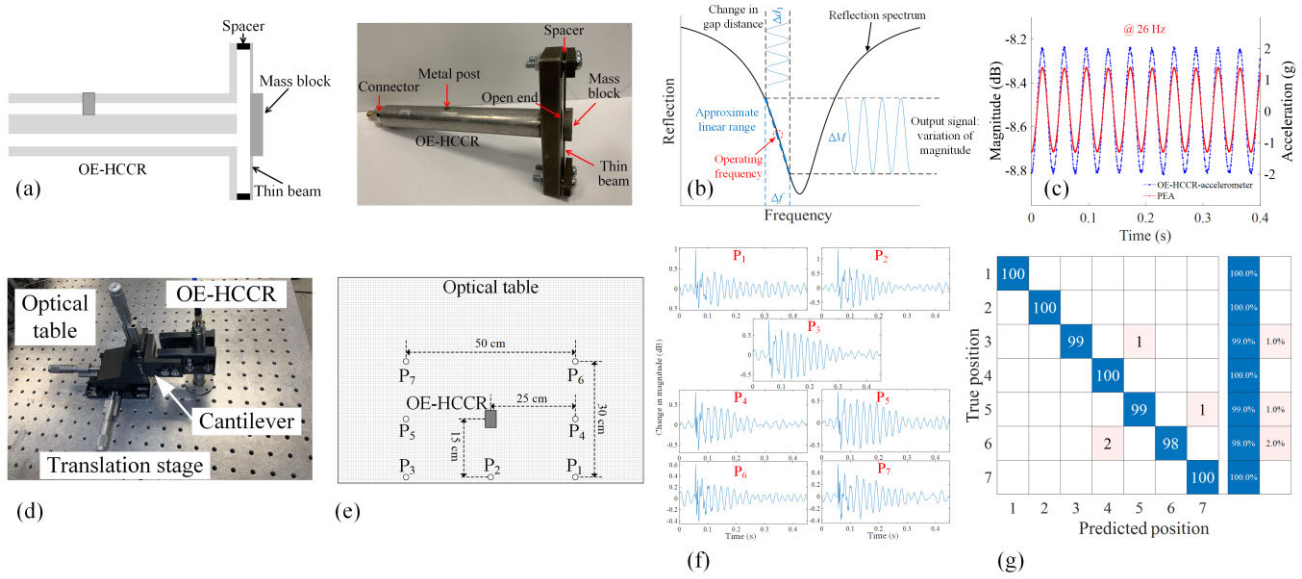

Fig. 15. OE-HCCR accelerometer [66]. (a) Schematic and photograph of a prototype device. (b) Illustration of the single-frequency interrogation approach. (c) Comparison between the OE-HCCR sensor and a commercial accelerometer when a 26-Hz signal is applied. (d) Photograph showing that an OE-HCCR is mounted on an optical table via a translation stage. (e) Top view schematic illustration showing that seven different positions are chosen on the surface of the optical table to demonstrate the capability of the OE-HCCR for predicting the locations of blunt-force impact events. (f) Examples of the time-transient responses of the OE-HCCR to vibrations caused by impact events at seven different locations shown in (e). (g) Confusion matrix showing prediction results from OE-HCCR intelligent system for classifying the locations of the impact events.

learning to sense impact events in 3-D space was demonstrated, as shown in Fig. 15(d)–(g). With machine learning-based analysis, the device is able to locate the position of an impact event that occurred near the sensor and the impactor implement according to the transient response of the sensor induced by the event. The harsh-environment compatibility (e.g., the performance of the sensor at elevated temperatures) should be further investigated.

Using a thin diaphragm as the external reflection mirror of an OE-HCCR device, an ultrasensitive pressure sensor with a resolution of 0.1 Pa was reported [67]. Fig. 16(a) gives the schematic and a photograph of the prototype sensor. Based on an improved all-metal design, the operating temperature of the pressure sensor was proved to be 1000 °C, as shown in Fig. 16(b), making it an excellent candidate in aerospace applications, e.g., for in situ SHM of aircraft engines. Employing a two-rope suspended solid pendulum as the tilt responsive element and the external reflector of the OE-HCCR, a high-performance inclinometer for measurements of tilt angles with the 110-nard resolution was demonstrated [68], as given in Fig. 16(c). It is noted that the resolution of the OE-HCCR inclinometer is approximately 70 times better than the HCC-FPR-based device [55] and is also comparable to an expensive fiber-optic EFPI inclinometer [69], demonstrating the potential of the OE-HCCR technique. Furthermore, extending the concept into a 2-D space, a 2-D inclinometer shown in Fig. 16(d) for the measurement of tilt angles along two orthogonal directions was proposed [68].

In addition to the air-gap distance, the OE-HCCR is also sensitive to variations of the dielectric property of the gap medium between the open end of the coaxial line and the metal plate, inherited from open-ended coaxial dielectric probes. The unique feature of the OE-HCCR is that the dielectric

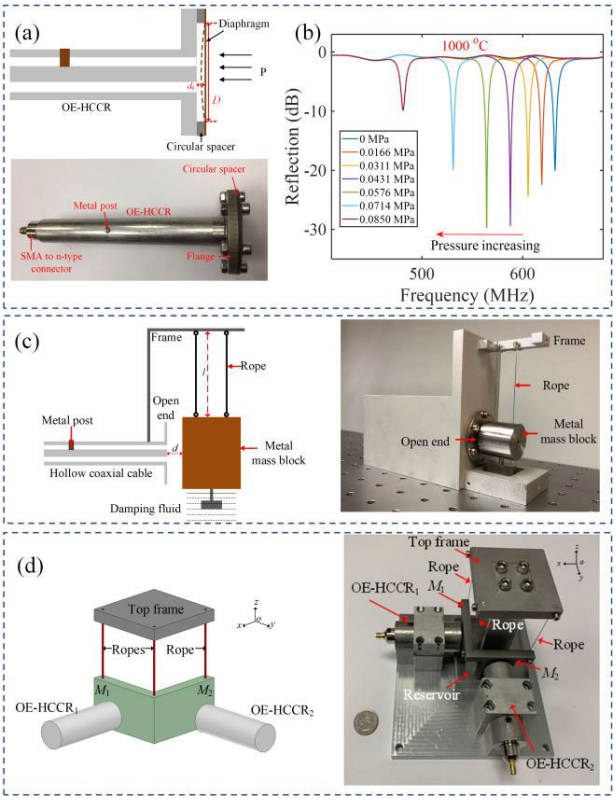

Fig. 16. OE-HCCR for pressure and tilt sensing. (a) Schematic and photograph of a diaphragm-based OE-HCCR pressure sensor [67]. (b) Responses of the OE-HCCR sensor to variations of pressure at 1000 °C [67]. (c) Schematic and photograph of a pendulum-based OE-HCCR tilt sensor [68]. (d) Schematic and photograph of a pendulum-based 2-D OE-HCCR tilt sensor [68].

sensitivity increases as the *pseudo* cavity length (the gap distance) decreases. Based on the enhanced dielectric sensitivity, an OE-HCCR-based fast-response hygrometer was developed

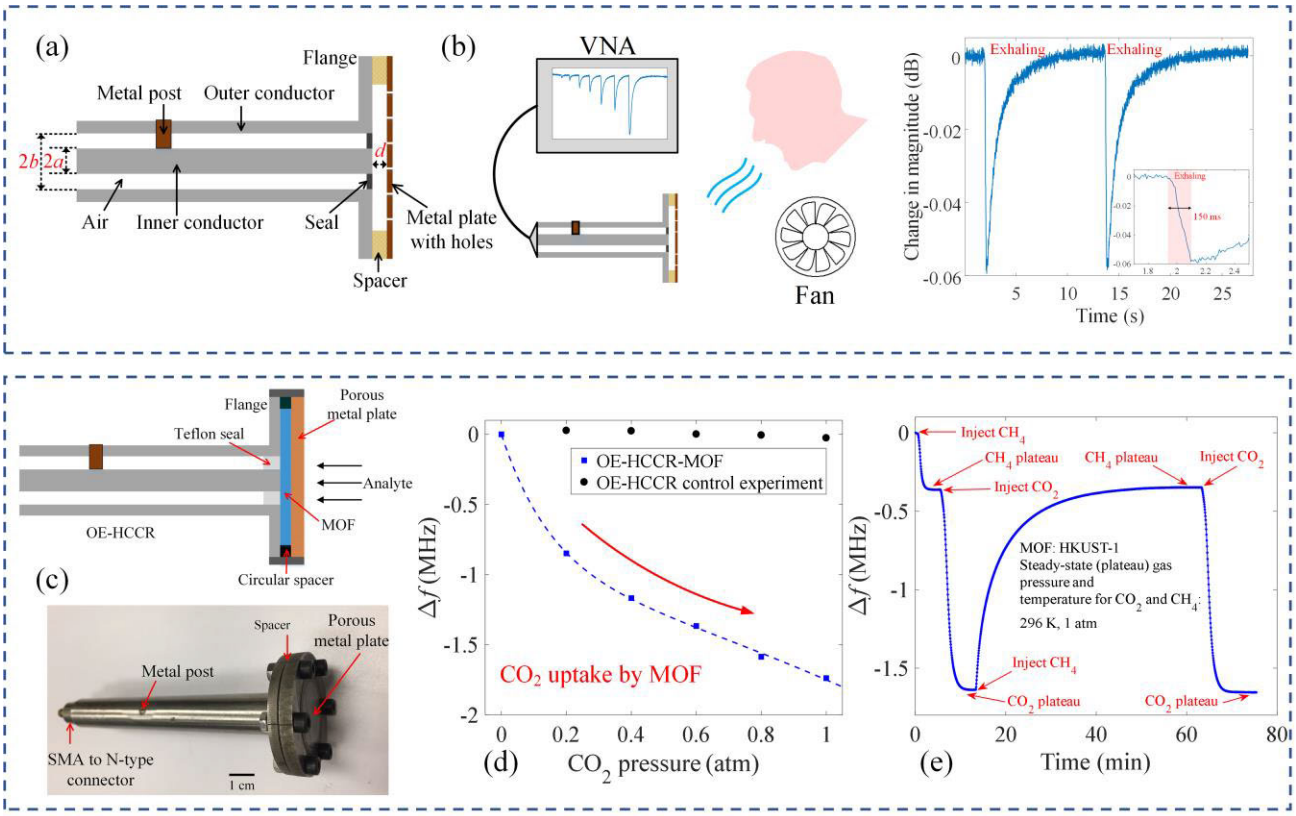

Fig. 17. OE-HCCR for biochemical sensing. (a) Schematic of an OE-HCCR humidity sensor [70]. (b) Schematic and responses of the OE-HCCR for real-time sensing human breath. (c) Schematic and photograph of an OE-HCCR-MOF gas sensor [72]. (d) Responses of the device to various concentrations of CO_2. The responses of a control OE-HCCR (without the MOF layer) are also included for comparison. (e) Demonstration test of the competitive gas adsorption between CH_4 and CO_2 of the OE-HCCR-MOF sensor.

for human breath sensing without using any hygroscopic material [70]. A porous metal plate is used to back the open end of the OE-HCCR, as shown in Fig. 17(a), such that human exhales could enter the *pseudo* cavity where the interaction between the localized electric field and the MUT occurs. Since no hygroscopic material is used, the sensor shows fast responses to variations of humidity, facilitating real-time sensing of human breath, as shown in Fig. 17(b). By inserting a polyvinyl alcohol film into the gap, an embeddable soil moisture sensor with high sensitivity was developed [71]. A portable gas sensor was developed by combining the chemical-specific adsorption properties of MOF materials with the improved dielectric sensitivity of the OE-HCCR [72]. A schematic and a photograph of the OE-HCCR-MOF device are shown in Fig. 17(c). A layer of MOF with a thickness of 200 μm is filled in the *pseudo* cavity of the OE-HCCR as the gas adsorption host. As shown in Fig. 17(d), the measurement sensitivity of the OE-HCCR-MOF device drastically improves because of the inclusion of the MOF layer. More importantly, the chemical selectivity of the OE-HCCR-MOF device is enhanced, as shown in Fig. 17(e), where the device shows high selectivity of CO_2 due to the fact that the MOF (HKUST-1) has a large adsorption propensity for CO_2. However, the temperature crosstalk of the device and the long-term stability of the OE-HCCR-MOF device need to be further investigated. Nevertheless, the OE-HCCR-MOF essentially provides a novel portable chemical sensing platform, which integrates the high sensitivity of OE-HCCR and the chemical selectivity of MOF materials. A series of chemically selective and sensitive gas sensors can be developed based on the OE-HCCR platform and different MOF materials tailored for different targets.

Further development and optimization of OE-HCCR-based sensor devices are ongoing in the Research Center for Optical Fiber Sensing, Zhejiang Laboratory, Hangzhou, China. The ultrahigh sensitivity, ease of fabrication, ease of signal interrogation, and high mechanical robustness of the OE-HCCR make it comparable to fiber-optic EFPI sensors, especially when it comes to sensing applications in harsh environments. The potential limitations of the OE-HCCR include its relatively large size and its susceptibility to EM interference.

V. Coaxial Cable Distributed Sensing

A. Cascaded CC-IFPI-Based

The CC-IFPIs discussed above have shown distinct advantages of large strain capability and mechanical robustness compared to the fiber-optic IFPIs, which are particularly attractive in SHM applications. Another desired feature of a sensing system for SHM is the ability of multi-point and/or distributed sensing. It is worth noting that multiple fiber-optic IFPIs can be cascaded along a single optical fiber for multipoint sensing, so-called multiplexed sensing [73]. The multiplexing capability of fiber-optic IFPIs has also prompted researchers to explore the distributed sensing capability of

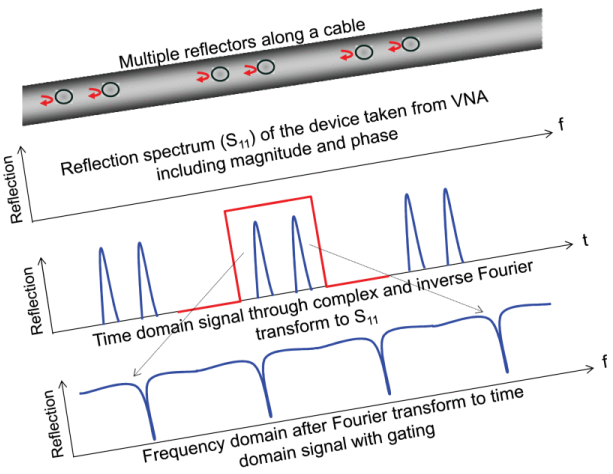

Fig. 18. Conceptual illustration of the joint time–frequency interrogation of cascaded CC-IFPIs for distributed sensing [74].

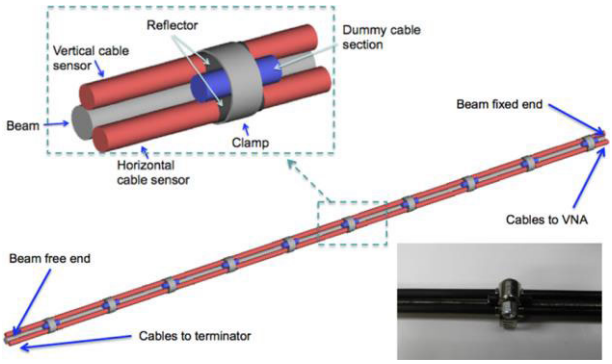

Fig. 19. Cascaded CC-IFPI-based shape sensor.

CC-IFPIs. Toward this end, a joint time–frequency technique was proposed to interrogate cascaded CC-IFPIs for truly distributed sensing [74], [75]. A conceptual illustration of the joint time–frequency interrogation is shown in Fig. 18. Multiple in-line reflectors are fabricated and cascaded along the coaxial cable. The complex transfer function of the system at a specific frequency (ω) can be measured from a VNA and can be expressed as [74]

$$H(\omega) = \sum_{i=1}^{N} \Gamma_i \exp j\left(-\frac{2z_i\sqrt{\varepsilon_r}}{c}\omega\right) \tag{24}$$

where Γ_i and z_i are the reflection coefficient magnitude and spatial location of the ith reflector along the coaxial cable; c is the speed of light in the vacuum; and ε_r is the relative permittivity of the dielectric layer. Applying an inverse Fourier transform to the transfer function $H(\omega)$, the impulse response of the system can be written as

$$\begin{aligned} h(t) &= \frac{1}{2\pi}\int_{\omega_{\min}}^{\omega_{\max}} H(\omega)\exp(j\omega t)d\omega \\ &= \sum_{i=1}^{N} \Gamma_i \sin c[(\omega_{\max}-\omega_{\min})(t-\tau_i)] \end{aligned} \tag{25}$$

where t is the time term; $\omega_{\max}$ and $\omega_{\min}$ are the maximum and minimal angular frequencies of the probing microwave signals; and τ_i is the time delay of the ith reflector and is given by

$$\tau_i = \frac{2z_i\sqrt{\varepsilon_r}}{c}. \tag{26}$$

Equation (25) reveals that the impulse response of a cascaded CC-IFPIs system is a superposition of a series of sinc functions, and the peak positions of each of the sinc functions correspond to the spatial location of each of the reflectors. Compared to multiplexed fiber-optic IFPIs, both the magnitude and phase spectra of the cascaded CC-IFPIs could be directly measured using a VNA, from which the rich-information impulse response can be obtained. Any two consecutive reflectors along the cable can be considered as a CC-IFPI, and the interferogram can be reconstructed by applying a time gate to the impulse response to select the two reflectors of interest [75]

$$H_S(\omega) = H(\omega) * \left[G(\omega)\exp(-j\omega\tau_o)\right] \tag{27}$$

where $G(\omega)$ is the inverse Fourier transform of the applied gate function and τ_o is the time delay of the gate. Then, the reconstructed interferogram can be used for localized sensing applications by tracking its spectra shift, as is the case for a single CC-IFPI shown in Section III. As a result, both the spatial location and the localized external perturbations on an arbitrary CC-IFPI along the cable can be obtained. By integrating the information from all the CC-IFPIs, distributed sensing can, thus, be achieved. The gauge length of each of the CC-IFPI can be flexibly designed in different applications. The spatial resolution of the system is limited by the frequency bandwidth of the probing microwave signals; the larger the bandwidth, the higher the spatial resolution.

Cascaded CC-IFPI-based distributed sensing was first demonstrated as an effective downhole monitoring technique for CO_2 sequestration due to its robust and low system cost [76], [77], [78], [79]. By correlating parameters of interest, e.g., torsion and beam shape, to spatially varying strain fields, distributed torsion sensing was demonstrated [80]. Using multiple coaxial cables with cascaded IFPIs to measure the strain distribution of a beam in the horizontal and vertical planes, the shape was successfully reconstructed based on a strain-displacement transfer scheme [81], [82]. The sensor arrangement is given in Fig. 19.

Smart civil structures with embedded cascaded CC-IFPIs were also reported with built-in capability for reliable and real-time monitoring of large strains and cracks [83], [84], [85]. A comparative study of using FBGs and CC-IFPIs for crack sensing was demonstrated in [84]. Instead of drilling a hole into a coaxial cable to create a reflector, crimping a cylindrical metal ferrule at a specific location on the cable is employed, as shown in Fig. 20(a). The reflectivity can be adjusted by varying the crimp length. Epoxy resin is then used to package each of the reflectors. A photograph of a prototype CC-IFPI-based distributed sensor fabricated based on an SF141 cable is given in Fig. 20(b). Fig. 20(c) gives the sensor layout on the bottom surface of a reinforced concrete specimen. The measurement results from different types of

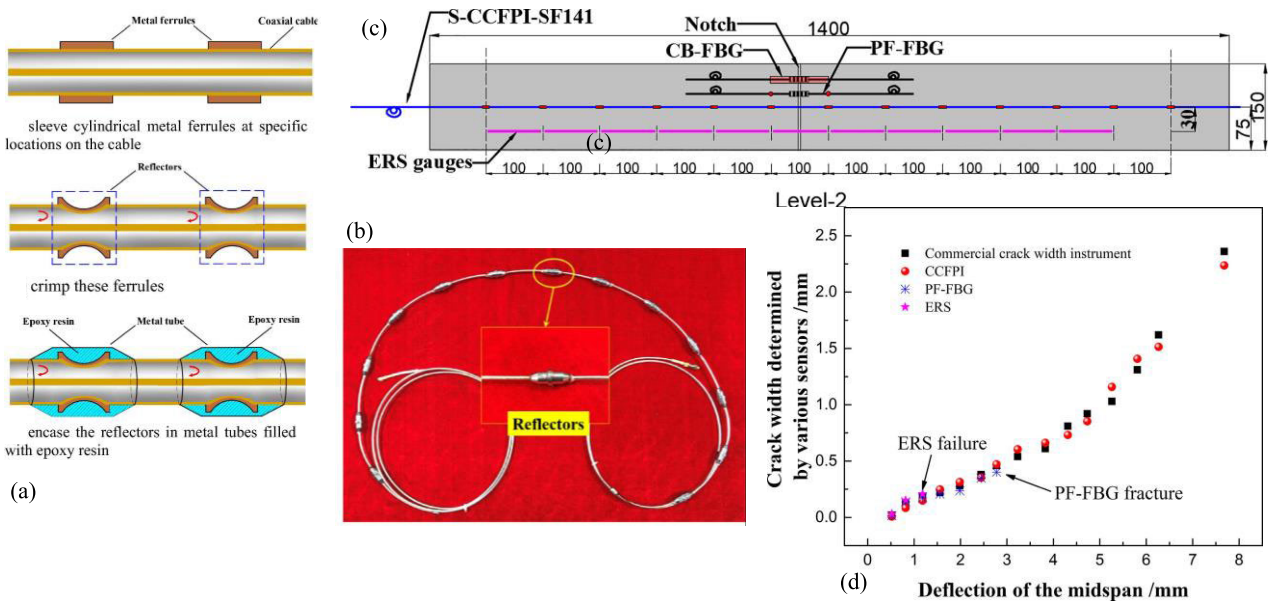

Fig. 20. Cascaded CC-IFPIs for crack sensing [84]. (a) Method of creating a CC-IFPI. (b) Photograph of a prototype CC-IFPI-based distributed sensor. (c) Schematic of the sensor layout in a reinforced concrete specimen. (d) Measurement results from different sensors bonded to the bottom surface of the specimen.

sensors are shown in Fig. 20(d). It is shown that the electrical resistance strain (ERS) gauge and the FBG sensor fail at a very early stage during the load experiment, whereas the CC-IFPIs show a surprisingly large dynamic range of up to 2.24 mm in terms of the measurable crack width with an error of ±0.15 mm. With a more proper bonding approach, the dynamic range of the CC-IFPIs can be further improved, showing great potential for large strain and crack sensing in extreme conditions. On the other hand, by cascading the aforementioned MCCC-IFPIs along a single metal-ceramic cable, a multipoint high-temperature sensor that could operate up to 1000 °C was reported and was demonstrated with a high measurement accuracy of ±3 °C [86]. Air gaps are used as the reflectors to construct the IFPI, and the reflection coefficient magnitude of the air-gap reflector on the air-gap distance is thoroughly studied, providing a guideline for further research to cascade a greater number of such IFPIs for covering longer sensing ranges.

B. Scattering-Based

In addition to multiplexed IFPI sensing, another widely used fiber-optic distributed sensing technique is based on the intrinsic Rayleigh scattering along an optical fiber [87]. Rayleigh backscattering in an optical fiber originates from random inhomogeneities along the length of the fiber, which are caused by random variations of refractive index frozen in the fiber core during the drawing/heating process when the fibers are manufactured [88]. The incident light travels along the fiber and encounters random fluctuations, therefore generating Rayleigh backscattering signals. The Rayleigh signals contain the spatial position information and the local profile of the index of refraction along the fiber. External perturbations (e.g., variations of temperature and strain) cause changes in the localized Rayleigh signals, which can be interpreted at the signal detection unit. Therefore, the inherent random inhomogeneities make an unmodified optical fiber a spatially distributed sensor. Interestingly, researchers have noted that the phenomenon of "backscattering" also existed in an unmodified coaxial cable, which is due to the fact that random impedance inhomogeneities are also embedded along a coaxial cable when it is manufactured, sourcing from fluctuations of the size dimensions of the inner/outer conductors, and the inhomogeneous density or permittivity profile of the dielectric layer. Therefore, inspired by the Rayleigh backscattering-based sensing technique in fiber-optic sensors, truly distributed coaxial cable sensing based on random impedance inhomogeneities was recently demonstrated [89], [90]. Compared to the cascaded CC-IFPIs, no additional reflectors are required in the inhomogeneity-based sensor, and thereby, the structural integrity of the coaxial cable is maintained. However, the SNR of the scattering-based system is lower than that of the cascaded CC-IFPIs system due to the low reflectivity of the spatially distributed random scattering points. In addition to sensing, a physical unclonable function technology based on the intrinsic impedance inhomogeneities of coaxial cables was reported [91], mimicking the idea of unclonable optical fiber identification (OFID) [92].

VI. Discussion

Over the past decade, a family of coaxial cable sensors has been developed, inspired by various fiber-optic sensors. A summary of the recently developed coaxial cable sensors is shown in Table I. CCBGs and CC-IFPIs fabricated from commercial flexible coaxial cables have been demonstrated for measurements of large strains, which enhance advanced approaches to SHM [24], [42]. With the implementation of the FPI configuration on homemade MCCCs and HCCs, a series of coaxial cable devices that can be used for sensing

TABLE I
SUMMARY OF COAXIAL CABLE SENSORS

Principle	Configuration	Advantages	Disadvantages
Fabry-Perot interference	Flexible cable-based intrinsic structure	Ease of fabrication Capability for large strain Capability for multiplexing	Low temperature tolerance Low sensitivity
	Hollow cable-based intrinsic structure	Ease of fabrication High mechanical strength High flexibility in material selection Capability for high temperature Capability for multiplexing Linear response Large dynamic range	Low sensitivity Large in size
	Hollow cable-based extrinsic structure	High sensitivity High flexibility in sensor design Capability for high temperature	Nonlinear response Limited dynamic range Pointwise sensor
Bragg grating	Flexible cable-based	Ease of fabrication Ease of signal demodulation Capability for large strain	Long gause length Low temperature tolerance
Scattering	Flexible cable-based	Truly distributed sensing Capability for large strain	Low signal-to-noise ratio Low temperature tolerance

applications at high temperatures have been developed [46], [53]. However, the existing MCCC-IFPIs and HCC-FPRs are made of stainless steel, and the temperature performance of these devices is demonstrated only to 1000 °C, which is far behind sapphire optical fiber sensors [44], [93]. We have noticed that, at elevated temperatures (>1000 °C), the SNR of the reflection spectra measured from a stainless-steel HCC-PFR degrades. The deterioration in the sensing signal might be due to the oxidation of the material (stainless steel) and increased resistance of the conductors caused by the increased kinetic energy of the atoms. Therefore, searching for suitable high-temperature materials (e.g., graphite and Tungsten) is crucial in the further development of high-temperature coaxial cable sensors.

Truly distributed coaxial cable sensors have also been demonstrated based on cascaded CC-IFPIs and random impedance inhomogeneities along a coaxial cable, mimicking their fiber-optic counterparts [74], [90]. Distributed coaxial cable sensors have been used in several practical applications, for example, for measurements of cracks and large strains in civil structures, downhole temperature, and strain monitoring [76], [84]. The fundamental basis of the distributed coaxial cable sensors is frequency-domain reflectometry (FDR). However, compared to distributed fiber-optic sensors, e.g., optical FDR (OFDR), the spatial resolution of coaxial cable sensors is compromised. The spatial resolution of an FDR system is mainly limited by the bandwidth of the microwave source. The frequency range of current low-cost microwave sources is limited to a few gigahertz, resulting in a low spatial resolution of several centimeters for a distributed coaxial cable sensor. Therefore, with the development of electronic components and microwave photonics, low-cost microwave sources with wider bandwidths will be developed to further improve the performance of coaxial cable distributed sensors. On the other hand, the joint time–frequency interrogation of distributed coaxial cable sensors involves complicated signal processing, limiting their temporal resolution. An advanced signal processing algorithm, e.g., based on phase demodulation, might be developed to increase both the temporal and spatial resolutions of distributed coaxial cable sensors.

A unique coaxial cable device, namely, the OE-HCCR, was reported very recently [65]. Apart from the features inherited from traditional coaxial cable sensors, the most salient point of the OE-HCCR is the ultrahigh sensitivity and resolution, three orders of magnitude greater than traditional coaxial cable sensors. Compared to a fiber-optic EFPI sensing system, an OE-HCCR system is featuring in its low cost (sensor fabrication and interrogator), ease of signal interrogation, improved mechanical robustness, and the potential for ultrahigh thermal stability. Currently, a VNA is typically employed to quantify the response of an OE-HCCR sensor. The system cost is expected to be largely reduced by building the bespoke electronics for the interrogator since only the reflection spectrum magnitude is needed for sensing applications. Thus, the OE-HCCR has paved the way to develop a novel generation of low-cost and ultrasensitive sensors that operate at a very low frequency (subgigahertz and gigahertz regimes). It is worth noting that the OE-HCCR functions based on the localized and enhanced fringing electric field at its open end, making it susceptible to EM interference. Meanwhile, the size dimension of an OE-HCCR is tens of times larger than a fiber-optic EFPI sensor. Future work can focus on the miniaturization of OE-HCCR sensors based on transmission line theory. Another promising direction is to integrate the OE-HCCR with a new phase shift amplification technique [94], [95], from which an unprecedented resolution from the OE-HCCR might be obtained, which could even surpass the performance of laser interferometry. However, the dynamic range might be compromised due to the highly nonlinear response.

With the circumstance of the Covid-19 pandemic, we have been striving to develop an OE-HCCR-based breath analyzer probe for the real-time survey of healthy and compromised lung function through breath matter content trapped in the

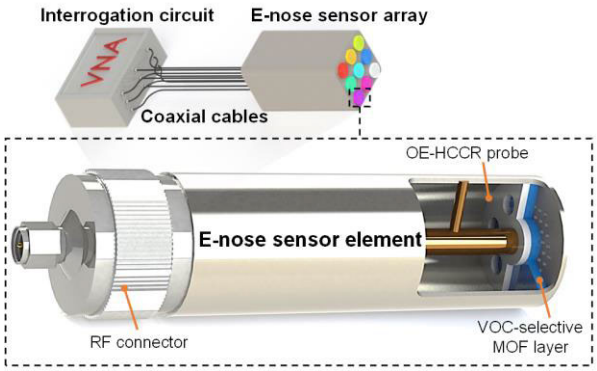

Fig. 21. Conceptual illustration of an OE-HCCR-based sensor array with different chemically selective layers for VOC sensing.

pseudo cavity of the OE-HCCR. We expect that the OE-HCCR probe will serve as an inexpensive, robust, and highly sensitive breath analyzer based on the hypothesis that volatile materials in exhaled breath (i.e., water vapor, nitrogen, and so on) will first dominate the sensing signal generated by the breath analyzer. However, due to their volatile nature, these materials quickly disperse, leaving only the offset signal generated by the nonvolatile particulates (i.e., virions) indicative of compromised lungs. To further improve the specificity of the OE-HCCR breath analyzer, an array of OE-HCCR with different functional materials (e.g., MOF) can be assembled to quantify volatile organic compounds (VOCs) in human breath for noninvasive diagnosis of diseases, as shown in Fig. 21, similar to the electronic nose technique [96]. Importantly, MOFs provide high surface areas, extraordinary regularities of their porosity, tailorable chemical properties, and reversible sorption characteristics, so they are encouraging candidates for adsorbent materials for gas and VOC sequestration [97]. Therefore, combining the chemical selectivity and reversibility of MOFs, the high sensitivity of OE-HCCR-based dielectric spectroscopy should provide a solution for in situ, reliable, low-cost, and rapid detection of target VOCs. Advanced analytical techniques, i.e., machine learning techniques, can be employed to achieve the complex mapping between the responses from the sensor array and the profiles of VOCs (i.e., specific diseases) based on intensive training and validation processes to further enhance the system performance [98], [99].

At last, it is worth noting that the discussed coaxial cable sensors have some unique features compared to other commonly reported microwave sensors, e.g., planar sensors. Indeed, planar sensors are one of the most widely developed microwave sensors because of their low profile, ease of integration, and versatility, and have undergone tremendous growth and advancement in recent years [100], [101], [102], [103]. Based on the EM interaction between the sensor and the MUT, planar sensors have mainly been used for material characterization by measuring the complex permittivity of the MUT at microwave frequencies. Different approaches have been explored to improve the sensitivity and selectivity of planar sensors [104], [105], [106], [107]. However, the application scope of planar microwave sensors has been fundamentally limited due to the working principle of this type of device. On the other hand, the coaxial cable sensors represent a new family of microwave sensors, and their applications have extended far beyond material characterization. The well-developed concept in fiber optic sensors can be readily translated into the microwave regime using the coaxial cable transmission line. As a result, various coaxial cable sensor devices have been successfully developed for measuring a diverse array of physical and chemical quantities, such as displacement, pressure, tilt angle, liquid level, acceleration, humidity, and gas concentration. Although the size of coaxial cable devices might be slightly larger than planar devices, they provide much higher flexibility in sensor design when the HCC platform is used. More importantly, the HCC device is an excellent candidate for sensing applications in high-temperature harsh environments. When combined with the EFPI configuration, it is expected that high-sensitivity sensors with high-temperature capability that are long desired can be potentially developed.

VII. Conclusion

Over the course of this review, recent progress in coaxial cable sensors has been considered. The CCBG and CC-IFPIs have been demonstrated with large strain capability, five times larger than that of the fiber-optic counterparts, which stands out as an attractive candidate for SHM applications. The MCCC-IFPIs and HCC-FPRs have been explored for high-temperature applications, striving to address the limitation encountered by the fiber-optic sensors at elevated temperatures. It is clear that much work is required to investigate the longevity and long-term stability of these coaxial cable sensors at elevated temperatures before their deployment in field applications. Despite the uncertainties, the MCCC-IFPIs and HCC-FPRs are invaluable platforms in the development of multiplexed, low-cost, reliable, and robust high-temperature sensors due to the fact that conducting materials with great thermal stability can be employed to construct these coaxial cable sensors. In addition to strain and temperature, other coaxial cables based on HCC-FPR have also been developed for the measurement of large-range displacement, liquid level, liquid interface, tilt angle, and so on, with highly linear responses and large dynamic ranges, as well as potential for high-temperature applications.

To address the limited resolution of HCC-FPR sensors, a unique configuration, i.e., the OE-HCCR, with record high measurement sensitivity and resolution among microwave sensors has been proposed, which might revolutionize the sensing field and facilitate a variety of sensing applications that have been long desired but are currently unavailable. Preliminary investigation has led to the successful development of high-performance sensors for highly sensitive measurements of a series of physical parameters, such as displacement, pressure, acceleration, and tilt angle, as well as biochemical quantities, including human breath and CO_2. It is envisioned that, by combining the OE-HCCR technique with more advanced transducer designs that have been demonstrated in the optical sensor field, a new generation of low-cost and ultrasensitive microwave sensors operating at subgigahertz regimes will emerge.

REFERENCES

[1] J. Hong Wang and K. K. Mei, "Theory and analysis of leaky coaxial cables with periodic slots," *IEEE Trans. Antennas Propag.*, vol. 49, no. 12, pp. 1723–1732, Dec. 2001.

[2] J. C. Beal, J. Josiak, S. F. Mahmoud, and V. Rawat, "Continuous-access guided communication (CAGC) for ground-transportation systems," *Proc. IEEE*, vol. 61, no. 5, pp. 562–568, May 1973.

[3] N. Nakamura, H. Tsunomachi, and R. Fukui, "Road vehicle communication system for vehicle control using leaky coaxial cable," *IEEE Commun. Mag.*, vol. 34, no. 10, pp. 84–89, Oct. 1996.

[4] H. Haag and K. Lehan, "Leaky coaxial cable systems for high speed trains in tunnels and other environmental conditions-theory and experience," in *Proc. 39th Int. Wire Cable Symp.*, Reno, NV, USA, Nov. 1990, pp. 71–79.

[5] K. Inomata, T. Hirai, K. Sumi, and K. Tanaka, "Wide-area surveillance sensor with leaky coaxial cables," in *Proc. SICE-ICASE Int. Joint Conf.*, Oct. 2006, pp. 959–963.

[6] K. Inomata, W. Tsujita, and T. Hirai, "2 in 1 leakey coaxial cable for intrusion detection sensor," in *Proc. IEEE Sensors Appl. Symp.*, Feb. 2013, pp. 76–79.

[7] K. Inomata, W. Tsujita, and T. Hirai, "Two-frequency surveillance technique for intrusion-detection sensor with leaky coaxial cables," in *Proc. IEEE Sensors Appl. Symp. (SAS)*, Feb. 2014, pp. 103–106.

[8] Q. Guan, C. Chen, and C. He, "A novel sensor using VHF zigzag-slotted leaky coaxial cable for intruder localization," *Microw. Opt. Technol. Lett.*, vol. 60, no. 3, pp. 634–639, Mar. 2018.

[9] S. A. Shah et al., "Posture recognition to prevent bedsores for multiple patients using leaking coaxial cable," *IEEE Access*, vol. 4, pp. 8065–8072, 2016.

[10] Z. Wang, A. Kiourti, and R. Lee, "A proximity sensor for the steering wheel based on leaky coaxial cable," *IEEE Sensors J.*, vol. 20, no. 24, pp. 14799–14808, Dec. 2020.

[11] C. P. Nemarich, "Time domain reflectometry liquid level sensors," *IEEE Instrum. Meas. Mag.*, vol. 4, no. 4, pp. 40–44, Dec. 2001.

[12] A. Cataldo, L. Tarricone, A. Trotta, F. Attivissimo, and C. Urso, "Time domain reflectometry technique for monitoring of liquid characteristics," in *Proc. IEEE Instrum. Meas. Technol. Conf.*, May 2005, pp. 1932–1936.

[13] S. Sun et al., "A novel TDR-based coaxial cable sensor for crack/strain sensing in reinforced concrete structures," *IEEE Trans. Instrum. Meas.*, vol. 58, no. 8, pp. 2714–2725, Aug. 2009.

[14] Z. Zhou, T. Jiao, P. Zhao, J. Liu, and H. Xiao, "Development of a distributed crack sensor using coaxial cable," *Sensors*, vol. 16, no. 8, p. 1198, Jul. 2016.

[15] G. D. Chen et al., "Crack detection of a full-scale reinforced concrete girder with a distributed cable sensor," *Smart Mater. Struct.*, vol. 14, no. 3, pp. S88–S97, May 2005.

[16] G. Chen, H. Mu, D. Pommerenke, and J. L. Drewniak, "Damage detection of reinforced concrete beams with novel distributed crack/strain sensors," *Struct. Health Monit.*, vol. 3, no. 3, pp. 225–243, Sep. 2004.

[17] G. J. Greene, A. Belarbi, and G. Chen, "Crack mapping in RC members using distributed coaxial cable crack sensors: Modeling and application," *Smart Struct. Syst.*, vol. 1, no. 4, pp. 385–404, Oct. 2005.

[18] S. Sun, D. J. Pommerenke, J. L. Drewniak, and G. Chen, "Signal loss, spatial resolution, and sensitivity of long coaxial crack sensors," *Proc. SPIE*, vol. 5391, pp. 786–797, Jul. 2014.

[19] M. A. Stuchly and S. S. Stuchly, "Coaxial line reflection methods for measuring dielectric properties of biological substances at radio and microwave frequencies—A review," *IEEE Trans. Instrum. Meas.*, vol. IM-29, no. 3, pp. 176–183, Sep. 1980.

[20] T. W. Athey, M. A. Stuchly, and S. S. Stuchly, "Measurement of radio frequency permittivity of biological tissues with an open-ended coaxial line: Part I," *IEEE Trans. Microw. Theory Techn.*, vol. MTT-30, no. 1, pp. 82–86, Jan. 1982.

[21] D. Popovic et al., "Precision open-ended coaxial probes for in vivo and ex vivo dielectric spectroscopy of biological tissues at microwave frequencies," *IEEE Trans. Microw. Theory Techn.*, vol. 53, no. 5, pp. 1713–1722, May 2005.

[22] B. L. McLaughlin and P. A. Robertson, "Miniature open-ended coaxial probes for dielectric spectroscopy applications," *J. Phys. D, Appl. Phys.*, vol. 40, no. 1, pp. 45–53, Dec. 2006.

[23] A. La Gioia et al., "Open-ended coaxial probe technique for dielectric measurement of biological tissues: Challenges and common practices," *Diagnostics*, vol. 8, no. 2, p. 40, Jun. 2018.

[24] J. Huang, T. Wei, X. Lan, J. Fan, and H. Xiao, "Coaxial cable Bragg grating sensors for large strain measurement with high accuracy," *Proc. SPIE*, vol. 8345, Apr. 2014, Art. no. 83452Z.

[25] S. J. Mihailov, "Fiber Bragg grating sensors for harsh environments," *Sensors*, vol. 12, no. 2, pp. 1898–1918, Feb. 2012.

[26] D. Kinet, P. Mégret, K. Goossen, L. Qiu, D. Heider, and C. Caucheteur, "Fiber Bragg grating sensors toward structural health monitoring in composite materials: Challenges and solutions," *Sensors*, vol. 14, no. 4, pp. 7394–7419, Apr. 2014.

[27] T. Wei, S. Wu, J. Huang, H. Xiao, and J. Fan, "Coaxial cable Bragg grating," *Appl. Phys. Lett.*, vol. 99, no. 11, Sep. 2011, Art. no. 113517.

[28] H. Xiao, J. Fan, T. Wei, and S. Wu, "Coaxial cable Bragg grating sensor," U.S. Patent 9 046 342, Jun. 2, 2015.

[29] A. Kersey et al., "Fiber grating sensors," *J. Lightw. Technol.*, vol. 15, no. 8, pp. 1442–1463, Aug. 1997.

[30] M. D. M. Sánchez-López, J. A. Davis, and K. Crabtree, "Coaxial cable analogs of multilayer dielectric optical coatings," *Amer. J. Phys.*, vol. 71, no. 12, pp. 1314–1319, Dec. 2003.

[31] S. Wu, T. Wei, J. Huang, H. Xiao, and J. Fan, "Modeling of coaxial cable Bragg grating by coupled mode theory," *IEEE Trans. Microw. Theory Techn.*, vol. 62, no. 10, pp. 2251–2259, Oct. 2014.

[32] S. Wu, T. Wei, J. Huang, H. Xiao, and J. Fan, "A study on Q-factor of CCBG sensors by coupled mode theory," *Proc. SPIE*, vol. 8345, Apr. 2012, Art. no. 834549.

[33] J. Huang, T. Wei, S. Wu, X. Lan, J. Fan, and H. Xiao, "Coaxial cable Bragg grating sensors for structural health monitoring," *Int. J. Pavement Res. Technol.*, vol. 5, no. 5, p. 338, Sep. 2012.

[34] J. Huang, T. Wei, X. Lan, J. Fan, and H. Xiao, "Coaxial cable Bragg grating sensors for large strain measurement with high accuracy," *Proc. SPIE*, vol. 8345, pp. 840–848, Apr. 2012.

[35] H. Tsuda, "Fiber Bragg grating vibration-sensing system, insensitive to Bragg wavelength and employing fiber ring laser," *Opt. Lett.*, vol. 35, no. 14, pp. 2349–2351, Jul. 2010.

[36] Z. Zhou, P. Li, Y. Li, P. Zhao, H. Xiao, and J. Ou, "Novel coaxial cable sensors for large strain measurement in SHM," in *Proc. Civil Struct. Monit. Workshop (CSHM)*, vol. 20, Nov. 2012.

[37] J. Fu, X. Wang, T. Wei, M. Wei, and Y. Shen, "A cost-effective geodetic strainmeter based on dual coaxial cable Bragg gratings," *Sensors*, vol. 17, no. 4, p. 842, Apr. 2017.

[38] J. Huang, "Coaxial cable Bragg grating," Tech. Rep., 2012.

[39] D. A. Usanov, S. A. Nikitov, A. V. Skripal, D. V. Ponomarev, O. M. Ruzanov, and I. O. Timofeev, "Application of a microwave coaxial Bragg structure for the measurement of parameters of insulators," *J. Commun. Technol. Electron.*, vol. 65, no. 5, pp. 541–548, May 2020.

[40] A. R. Nasybullin, O. G. Morozov, G. A. Morozov, R. V. Farkhutdinov, P. V. Gavrilov, and I. A. Makarov, "Means for monitoring the dielectric parameters of liquid media based on quasiperiodic Bragg microwave structures in a coaxial waveguide," *J. Phys., Conf. Ser.*, vol. 1499, no. 1, Mar. 2020, Art. no. 012015.

[41] O. G. Morozov, A. R. Nasybullin, M. P. Danilaev, and R. V. Farkhutdinov, "Sensor applications of Bragg microwave structures realized in coaxial waveguide," in *Proc. Int. Conf. Antenna Theory Techn. (ICATT)*, Apr. 2015, pp. 1–3.

[42] J. Huang, T. Wang, L. Hua, J. Fan, H. Xiao, and M. Luo, "A coaxial cable Fabry–Pérot interferometer for sensing applications," *Sensors*, vol. 13, no. 11, pp. 15252–15260, Nov. 2013.

[43] T. Wei, Y. Han, H.-L. Tsai, and H. Xiao, "Miniaturized fiber inline Fabry–Pérot interferometer fabricated with a femtosecond laser," *Opt. Lett.*, vol. 33, no. 6, pp. 536–538, Mar. 2008.

[44] C. Zhu, R. E. Gerald, and J. Huang, "Progress toward sapphire optical fiber sensors for high-temperature applications," *IEEE Trans. Instrum. Meas.*, vol. 69, no. 11, pp. 8639–8655, Nov. 2020.

[45] H. Chen, M. Buric, P. R. Ohodnicki, J. Nakano, B. Liu, and B. T. Chorpening, "Review and perspective: Sapphire optical fiber cladding development for harsh environment sensing," *Appl. Phys. Rev.*, vol. 5, no. 1, Mar. 2018, Art. no. 011102.

[46] A. Trontz, B. Cheng, S. Zeng, H. Xiao, and J. Dong, "Development of metal-ceramic coaxial cable Fabry–Pérot interferometric sensors for high temperature monitoring," *Sensors*, vol. 15, no. 10, pp. 24914–24925, Sep. 2015.

[47] C. Zhu, Y. Chen, Y. Zhuang, and J. Huang, "Displacement and strain measurement up to 1000 °C using a hollow coaxial cable Fabry–Pérot resonator," *Sensors*, vol. 18, no. 5, p. 1304, Apr. 2018.

[48] D. M. Pozar, *Microwave Engineering*. Hoboken, NJ, USA: Wiley, 2009.

[49] M. F. Ahmed, T. Xue, B. Wu, and J. Huang, "High quality factor coaxial cable Fabry–Pérot resonator for sensing applications," *IEEE Sensors J.*, vol. 17, no. 10, pp. 3052–3057, May 2017.

[50] C. Zhu, Y. Chen, Y. Zhuang, and J. Huang, "A centimeter-range displacement sensor based on a hollow coaxial cable Fabry–Pérot resonator," *IEEE Sensors J.*, vol. 18, no. 11, pp. 4436–4442, Jun. 2018.

[51] C. Zhu, R. E. Gerald, Y. Chen, and J. Huang, "Probing the theoretical ultimate limit of coaxial cable sensing: Measuring nanometer-scale displacements," *IEEE Trans. Microw. Theory Techn.*, vol. 68, no. 2, pp. 816–823, Feb. 2020.

[52] C. Zhu and J. Huang, "Wide-range displacement sensor based on a hollow coaxial cable Fabry–Pérot resonator," *Proc. SPIE*, vol. 10598, Apr. 2018, Art. no. 105983O.

[53] C. Zhu and J. Huang, "Displacement and strain measurement up to 1000 °C using a hollow coaxial cable Fabry–Pérot resonator," *Proc. SPIE*, vol. 11000, May 2019, Art. no. 110000M.

[54] C. Zhu, Y. Zhuang, Y. Chen, and J. Huang, "A liquid-level sensor based on a hollow coaxial cable Fabry–Pérot resonator with micrometer resolution," *IEEE Trans. Instrum. Meas.*, vol. 67, no. 12, pp. 2892–2897, Dec. 2018.

[55] J. Guo, C. Zhu, Y. Tang, and J. Huang, "Temperature-insensitive inclinometer based on transmission line Fabry–Pérot resonators," *IEEE Trans. Instrum. Meas.*, vol. 71, pp. 1–10, 2022.

[56] C. Zhu, Y. Zhuang, Y. Chen, and J. Huang, "A hollow coaxial cable Fabry–Pérot resonator for liquid dielectric constant measurement," *Rev. Sci. Instrum.*, vol. 89, no. 4, Apr. 2018, Art. no. 045003.

[57] S. Zeng, A. Trontz, W. Zhu, H. Xiao, and J. Dong, "A metal-ceramic coaxial cable Fabry–Pérot microwave interferometer for monitoring fluid dielectric constant," *Sens. Actuators A, Phys.*, vol. 257, pp. 1–7, Apr. 2017.

[58] B. Cheng, L. Yuan, W. Zhu, Y. Song, and H. Xiao, "A coaxial cable magnetic field sensor based on ferrofluid filled Fabry–Pérot interferometer structure," *Sens. Actuators A, Phys.*, vol. 257, pp. 194–197, Apr. 2017.

[59] C. Zhu, Y. Zhuang, Y. Chen, B. Zhang, and J. Huang, "Contactless liquid interface measurement based on a hollow coaxial cable resonator," *Sens. Actuators A, Phys.*, vol. 285, pp. 623–627, Jan. 2019.

[60] S. Zeng, A. Trontz, H. Xiao, and J. Dong, "Determining dielectric constants for complex solvent mixtures by microwave sensing and model prediction," *J. Phys. Chem. A*, vol. 125, no. 47, pp. 10245–10254, Nov. 2021.

[61] S. Zeng, A. Trontz, Z. Cao, H. Xiao, and J. Dong, "Characterizing the gas adsorption-dependent dielectric constant for silicalite nanoparticles at microwave frequencies by a coaxial cable Fabry–Pérot interferometric sensing method," *Madridge J. Nanotechnol. Nanosci.*, vol. 3, pp. 100–107, May 2018.

[62] C. Zhu, R. E. Gerald, and J. Huang, "Metal-organic framework materials coupled to optical fibers for chemical sensing: A review," *IEEE Sensors J.*, vol. 21, no. 18, pp. 19647–19661, Sep. 2021.

[63] S. Jenkins, A. G. P. Warham, and R. N. Clarke, "Use of open-ended coaxial line sensor with a laminar or liquid dielectric backed by a conducting plane," *IEE Proc. H, Microw., Antennas Propag.*, vol. 139, pp. 179–182, Apr. 1992.

[64] S. Fan, K. Staebell, and D. Misra, "Static analysis of an open-ended coaxial line terminated by layered media," *IEEE Trans. Instrum. Meas.*, vol. 39, no. 2, pp. 435–437, Apr. 1990.

[65] C. Zhu, R. E. Gerald, and J. Huang, "Microwave device inspired by fiber-optic extrinsic Fabry–Pérot interferometer: A novel ultra-sensitive sensing platform," *J. Lightw. Technol.*, vol. 38, no. 24, pp. 6961–6966, Dec. 15, 2020.

[66] C. Zhu, Y. Chen, R. E. Gerald, and J. Huang, "Ultrasensitive open-ended coaxial cable-based microwave resonator learns to sense impacts," *IEEE Trans. Instrum. Meas.*, vol. 70, pp. 1–9, 2021.

[67] C. Zhu, Y. Tang, J. Guo, R. E. Gerald, and J. Huang, "High-temperature and high-sensitivity pressure sensors based on microwave resonators," *IEEE Sensors J.*, vol. 21, no. 17, pp. 18781–18792, Sep. 2021.

[68] C. Zhu, Y. Tang, Y. Zhuang, J. Guo, R. E. Gerald, and J. Huang, "2-D tilt sensor based on coaxial cable Fabry–Pérot resonators with submicroradian resolution," *IEEE Trans. Microw. Theory Techn.*, vol. 70, no. 4, pp. 2398–2406, Apr. 2022.

[69] Y. Zhuang, Y. Chen, C. Zhu, R. E. Gerald, and J. Huang, "Probing changes in tilt angle with 20 nanoradian resolution using an extrinsic Fabry–Pérot interferometer-based optical fiber inclinometer," *Opt. Exp.*, vol. 26, no. 3, pp. 2546–2556, Feb. 2018.

[70] C. Zhu, R. E. Gerald, and J. Huang, "Highly sensitive open-ended coaxial cable-based microwave resonator for humidity sensing," *Sens. Actuators A, Phys.*, vol. 314, Oct. 2020, Art. no. 112244.

[71] J. Guo, Y. Tang, Y. Wu, C. Zhu, and J. Huang, "Embeddable soil moisture content sensor based on open-end microwave coaxial cable resonator," *IEEE Sensors J.*, vol. 23, no. 12, pp. 13575–13584, Jun. 2023.

[72] C. Zhu, R. E. Gerald, Y. Chen, and J. Huang, "Metal-organic framework portable chemical sensor," *Sens. Actuators B, Chem.*, vol. 321, Oct. 2020, Art. no. 128608.

[73] M. Wang et al., "Multiplexable high-temperature stable and low-loss intrinsic Fabry–Pérot in-fiber sensors through nanograting engineering," *Opt. Exp.*, vol. 28, no. 14, pp. 20225–20235, Jul. 2020.

[74] J. Huang et al., "Interferogram reconstruction of cascaded coaxial cable Fabry–Pérot interferometers for distributed sensing application," *IEEE Sensors J.*, vol. 16, no. 11, pp. 4495–4500, Jun. 2016.

[75] H. Xiao, J. Huang, X. Lan, and M. Luo, "Distributed microwave Fabry–Pérot interferometer device and method," U.S. Patent 9 534 937, Jan. 3, 2017.

[76] Y. Li, R. Nygaard, W. Zhu, and H. Xiao, "Robust and cost effective distributed coaxial cable temperature sensor verified as real-time permanent downhole monitoring for groundwater safety in geological CO_2 storage," in *Proc. Carbon Manag. Technol. Conf.*, Nov. 2015, Paper CMTC-438055.

[77] Y. Li, B. Cheng, W. Zhu, H. Xiao, and R. Nygaard, "Development and evaluation of the coaxial cable casing imager: A cost-effective solution to real-time downhole monitoring for CO_2 sequestration wellbore integrity," *Greenhouse Gases, Sci. Technol.*, vol. 7, no. 5, pp. 927–941, Oct. 2017.

[78] Y. Li, W. Zhu, B. Cheng, R. Nygaard, and H. Xiao, "Laboratory evaluation of distributed coaxial cable temperature sensors for application in CO_2 sequestration well characterization," *Greenhouse Gases, Sci. Technol.*, vol. 6, no. 6, pp. 812–823, Dec. 2016.

[79] Y. Li, R. Nygaard, B. Cheng, W. Zhu, and H. Xiao, "Laboratory evaluation of a real-time coaxial cable casing imager for wellbore integrity monitoring," in *Proc. 4th Unconventional Resour. Technol. Conf.* Houston, TX, USA: Society of Exploration Geophysicists, 2016, pp. 75–89.

[80] B. Cheng et al., "Distributed torsion sensor based on cascaded coaxial cable Fabry–Pérot interferometers," *Meas. Sci. Technol.*, vol. 27, no. 7, May 2016, Art. no. 075103.

[81] B. Cheng, W. Zhu, J. Liu, L. Yuan, and H. Xiao, "3D beam shape estimation based on distributed coaxial cable interferometric sensor," *Smart Mater. Struct.*, vol. 26, no. 3, Feb. 2017, Art. no. 035017.

[82] T. Wei, Z. Chen, and G. Hefferman, "Coaxial cable sensor device for distributed strain measurement and shape sensing applications," U.S. Patent 10 309 843, Jun. 4, 2019.

[83] T. Jiao, Z. Zhou, J. Liu, H. Xiao, and J. Ou, "Large strain-tolerated smart steel strand with built in coaxial cable Fabry–Pérot interferometer," *Measurement*, vol. 151, Feb. 2020, Art. no. 107019.

[84] T. Jiao, Z. Zhou, and H. Xiao, "Investigation into coaxial cable Fabry–Pérot interferometers for strain measurement and crack detection in RC structures," *Measurement*, vol. 147, Dec. 2019, Art. no. 106873.

[85] T. Jiao and Z. Zhou, "An optical-electrical co-sensing tape for cross-sectional deformation monitoring of shield tunnels," *Tunnelling Underground Space Technol.*, vol. 117, Nov. 2021, Art. no. 104148.

[86] A. Trontz, S. Zeng, B. Cheng, H. Xiao, and J. Dong, "A metal-ceramic coaxial cable with multipoint Fabry–Pérot interferometers for monitoring distributed high temperature," *Measurement*, vol. 162, Oct. 2020, Art. no. 107943.

[87] C. Zhu, Y. Zhuang, Y. Chen, R. E. Gerald, and J. Huang, "Distributed fiber-optic pressure sensor based on Bourdon tubes metered by optical frequency-domain reflectometry," *Proc.* , vol. 58, no. 7, Jul. 2019, Art. no. 072010.

[88] R. Juškaitis, A. M. Mamedov, V. T. Potapov, and S. V. Shatalin, "Distributed interferometric fiber sensor system," *Opt. Lett.*, vol. 17, no. 22, pp. 1623–1625, Nov. 1992.

[89] C. Zhu, Y. Zhuang, Y. Chen, and J. Huang, "Truly distributed coaxial cable sensing based on random inhomogeneities," *IEEE Trans. Instrum. Meas.*, vol. 68, no. 11, pp. 4600–4607, Nov. 2019.

[90] B. Cheng, L. Hua, W. Zhu, Q. Zhang, J. Lei, and H. Xiao, "Distributed temperature sensing with unmodified coaxial cable based on random reflections in TDR signal," *Meas. Sci. Technol.*, vol. 30, no. 1, Dec. 2018, Art. no. 015105.

[91] T. Wei and J. Huang, "Transmission line identification via impedance inhomogeneity pattern," *IEEE J. Radio Freq. Identificat.*, vol. 3, no. 4, pp. 245–251, Dec. 2019.

[92] Y. Du, S. Jothibasu, Y. Zhuang, C. Zhu, and J. Huang, "Unclonable optical fiber identification based on Rayleigh backscattering signatures," *J. Lightw. Technol.*, vol. 35, no. 21, pp. 4634–4640, Nov. 1, 2017.

[93] B. Wang, Y. Niu, X. Qin, Y. Yin, and M. Ding, "Review of high temperature measurement technology based on sapphire optical fiber," *Measurement*, vol. 184, Nov. 2021, Art. no. 109868.

[94] M. Ben Ayun, S. Rosenberg, D. Gotliv, and S. Sternklar, "Fundamental limits of photonic RF phase-shift amplification by RF interferometry," *J. Lightw. Technol.*, vol. 35, no. 10, pp. 1906–1913, May 15, 2017.

[95] C. Zhu, R. E. Gerald, and J. Huang, "On the sensitivity of microwave Fabry–Pérot interferometers for displacement detection," *IEEE Trans. Microw. Theory Techn.*, vol. 70, no. 8, pp. 3943–3953, Aug. 2022.

[96] F. Röck, N. Barsan, and U. Weimar, "Electronic nose: Current status and future trends," *Chem. Rev.*, vol. 108, no. 2, pp. 705–725, Feb. 2008.

[97] L. E. Kreno, K. Leong, O. K. Farha, M. Allendorf, R. P. Van Duyne, and J. T. Hupp, "Metal–organic framework materials as chemical sensors," *Chem. Rev.*, vol. 112, no. 2, pp. 1105–1125, Feb. 2012.

[98] S. Das and M. Pal, "Review—Non-Invasive monitoring of human health by exhaled breath analysis: A comprehensive review," *J. Electrochem. Soc.*, vol. 167, no. 3, Feb. 2020, Art. no. 037562.

[99] S. Lekha and M. Suchetha, "Recent advancements and future prospects on e-nose sensors technology and machine learning approaches for non-invasive diabetes diagnosis: A review," *IEEE Rev. Biomed. Eng.*, vol. 14, pp. 127–138, 2021.

[100] J. Muñoz-Enano, P. Vélez, M. Gil, and F. Martín, "Planar microwave resonant sensors: A review and recent developments," *Appl. Sci.*, vol. 10, no. 7, p. 2615, Apr. 2020.

[101] N. A. Rahman, Z. Zakaria, R. A. Rahim, Y. Dasril, and A. A. M. Bahar, "Planar microwave sensors for accurate measurement of material characterization: A review," *TELKOMNIKA, Telecommun. Comput. Electron. Control*, vol. 15, no. 3, pp. 1108–1118, 2017.

[102] C. G. Juan, B. Potelon, C. Quendo, and E. Bronchalo, "Microwave planar resonant solutions for glucose concentration sensing: A systematic review," *Appl. Sci.*, vol. 11, no. 15, p. 7018, Jul. 2021.

[103] J. Muñoz-Enano et al., "Planar phase-variation microwave sensors for material characterization: A review and comparison of various approaches," *Sensors*, vol. 21, no. 4, p. 1542, Feb. 2021.

[104] M. Abdolrazzaghi, V. Nayyeri, and F. Martin, "Techniques to improve the performance of planar microwave sensors: A review and recent developments," *Sensors*, vol. 22, no. 18, p. 6946, Sep. 2022.

[105] M. Abdolrazzaghi and M. Daneshmand, "Exploiting sensitivity enhancement in micro-wave planar sensors using intermodulation products with phase noise analysis," *IEEE Trans. Circuits Syst. I, Reg. Papers*, vol. 67, no. 12, pp. 4382–4395, Dec. 2020.

[106] N. Kazemi, M. Abdolrazzaghi, and P. Musilek, "Comparative analysis of machine learning techniques for temperature compensation in microwave sensors," *IEEE Trans. Microw. Theory Techn.*, vol. 69, no. 9, pp. 4223–4236, Sep. 2021.

[107] L. Harrsion, M. Ravan, D. Tandel, K. Zhang, T. Patel, and R. K. Amineh, "Material identification using a microwave sensor array and machine learning," *Electronics*, vol. 9, no. 2, p. 288, Feb. 2020.

Chen Zhu (Member, IEEE) received the B.E. degree in optoelectronics information engineering from the Huazhong University of Science and Technology, Wuhan, China, in 2015, and the Ph.D. degree in electrical engineering from the Missouri University of Science and Technology, Rolla, MO, USA, in 2021.

He is currently a Principal Investigator with the Research Center for Optical Fiber Sensing, Zhejiang Laboratory, Hangzhou, China. He has authored or coauthored over 60 refereed articles, 20 conference papers, and one book chapter. His research interest is focused on the development of fiber optic and microwave devices for sensing applications in harsh environments.

Dr. Zhu was a recipient of the IEEE Instrumentation and Measurement Society Graduate Fellowship Awards in 2018 and 2019, and the 2020 IEEE St. Louis Section Outstanding Graduate Student Award.

Jie Huang (Senior Member, IEEE) received the Ph.D. degree in electrical engineering from Clemson University, Clemson, SC, USA, in 2015.

He is currently the Roy A. Wilkens Endowed Associate Professor of electrical and computer engineering with the Missouri University of Science and Technology, Rolla, MO, USA. He has established the Lightwave Technology Laboratory, Rolla, with a strong track record of sustained research funding, high-quality journal publications, and state-of-the-art research infrastructures with cutting-edge capabilities. He has authored or coauthored more than 100 refereed articles, 70 conference papers, one book chapter, and ten U.S. patent applications in the area of advanced sensors. His research interests include the development of optical and microwave sensors and instrumentation for applications in energy, intelligent infrastructures, clean environments, biomedical sensing, and harsh environments.